

Gravity wave radiation from vortex trains in rotating shallow water

By RUPERT FORD†

Centre for Atmospheric Science, Department of Applied Mathematics and Theoretical Physics,
University of Cambridge, Silver Street, Cambridge, CB3 9EW, UK

(Received 10 March 1994 and in revised form 1 July 1994)

Gravity wave radiation by vortical flows in the f -plane shallow-water equations is investigated by direct nonlinear numerical simulation. The flows considered are initially parallel flows, consisting of a single strip in which the potential vorticity differs from the background value. The flows are unstable to the barotropic instability mechanism, and roll up into a train of vortices. During the subsequent evolution of the vortex train, gravity waves are radiated. In the limit of small Froude number, the gravity wave radiation is compared with that predicted by an appropriately modified version of the Lighthill theory of aerodynamic sound generation. It is found that the gravity wave field agrees well with that predicted by the theory, provided typical lengthscales of vortical motions are well within one deformation radius.

It is found that the nutation time for vortices in the train increases rapidly with increasing Froude number in cases where the potential vorticity in the vortices is of the same sign as the background value, whereas the nutation time is almost independent of Froude number in cases where the potential vorticity in the vortices is zero or of opposite sign to the background. Consequently, in the former cases, the unsteadiness of the flow decreases with increasing Froude number, so the effect of the inertial cut-off frequency is increased, leading to an optimal Froude number for gravity wave radiation, above which the intensity of the radiated waves decreases as the Froude number is further increased. It is proposed that the existence of a finite range of interaction within the vortices, for flows with positive vortex potential vorticity, may account for the strong dependence of nutation time on Froude number in those cases. The interaction scale within the vortices becomes infinite in the limit of zero vortex potential vorticity, and so the arguments do not apply in those cases.

1. Introduction

The remarkable extent to which vortical motions and gravity waves appear to have almost negligible interaction with each other in many cases of meteorological and oceanographic interest has received renewed attention in recent years, following the review article of Hoskins, McIntyre & Robertson (1985). The conceptual simplification of ‘balanced’ dynamics, in which, in the case of the shallow-water equations, the potential vorticity field alone is required to determine the evolution of the flow, and from which freely propagating gravity waves are therefore excluded (Hoskins *et al.* 1985; Ford, McIntyre & Norton 1994), makes it imperative that we understand precisely the circumstances in which vortical motions do excite strong gravity waves, and those in which they do not.

† Current address: Scripps Institution of Oceanography, 9500 Gilman Drive, La Jolla, CA92093-0225, USA.

Several numerical studies (McWilliams, Gent & Norton 1986; Norton 1988; Allen, Barth & Newberger 1990; Barth, Allen & Newberger 1990; McIntyre & Norton 1994) have addressed the degree to which various balanced models, of greater or lesser accuracy, given a variety of balanced initial conditions, will follow the evolution of the full equations from which gravity waves are not excluded. In particular, Norton (1988) and McIntyre & Norton (1994) demonstrate that gravity waves of large amplitude are generally not excited in shallow-water simulations of a forced stratospheric polar vortex, even when the Rossby number exceeds unity and the Froude number is of order unity in at least some parts of the domain.

However, using such an approach, it is very difficult to separate fundamentally unbalanced motions from corrections to the balanced dynamics not represented by the balanced model under consideration. The present paper therefore takes a somewhat different approach to the problem, and investigates the amplitude of freely propagating gravity waves generated by vortical motions in a flow in which the vortical flow is confined to a finite region, away from which gravity waves may radiate. The magnitude of the gravity wave fluxes far from the vortical region then serves as a measure of the degree to which the flow cannot be described in terms of balanced dynamics.

The model system of equations used in this study are the shallow-water equations on an f -plane (equations (1) and (2) below), which are the simplest equations in which both vortical motions and gravity waves can exist. In addition to their simplicity, a further advantage of the shallow-water equations is that, in the absence of the Coriolis force, they are equivalent to the equations for a two-dimensional adiabatic gas with a ratio of specific heats $\gamma = 2$. The gravity waves in the shallow-water equations are the analogues of the acoustic waves in the compressible gas equations. In this paper, we shall exploit this analogy, with specific reference to the Lighthill theory of aerodynamic sound generation (Lighthill 1952), in which vortical motions are regarded as responsible for the generation of sound waves. The theory predicts that, in the limit of small Mach number, the intensity of the acoustic waves radiated is proportional to M^{5+n} , where n is the number of spatial dimensions in which the acoustic waves propagate (Lighthill 1952; Ffowcs Williams 1969).

Since the development of the Lighthill theory of aerodynamic sound generation, several attempts have been made to verify it, and to investigate the range of Mach numbers over which it is valid. In general, acoustic data from three-dimensional jet experiments (Lighthill 1954; Lush 1971; Moore 1977; Bridges & Hussain 1992), two-dimensional jet experiments (Webster 1970) and three-dimensional vortex ring experiments (Kambe & Minota 1981, 1983; Minota & Kambe 1986) are in good agreement with the scaling laws, up to $M \approx 1$. Recently, Lele & Ho (1994) have presented a numerical study of a compressible mixing layer in a two-dimensional numerical model. The mixing layer is unstable, and the waves which grow on the edges of the mixing layer eventually develop into a train of coherent vortices. Lele & Ho found that the agreement between the simulated radiated wave field and its reconstruction using the Lighthill theory was quite good at Mach numbers of up to about 0.6, at which they found errors in the acoustic pressure field predicted by the Lighthill reconstruction of about 10%. For Mach numbers up to 0.2, the errors were only about 1–2%. Much larger errors were found, however, when the source flow was assumed to be incompressible. It seems that the low-Mach-number approximation is significantly violated in the vortical region at quite small Mach numbers, whereas the assumption that the source region is small compared with the scale of the acoustic waves generated, although formally a low-Mach-number approximation itself, is valid over a much wider range of Mach numbers.

In common with the study of Lele & Ho, the initial states for the present study are also unstable steady parallel shear flows, in which the flow is at rest far from the region of shear instability, with rest depth h_0 . However, the present study uses the f -plane shallow-water equations, so the effects of background rotation, relevant in the geophysical context of gravity wave generation, may be investigated. The f -plane shallow-water equations are

$$\frac{\partial \mathbf{u}}{\partial t} + \mathbf{u} \cdot \nabla \mathbf{u} + f \mathbf{k} \times \mathbf{u} + g \nabla h = 0, \quad (1)$$

$$\frac{\partial h}{\partial t} + \nabla \cdot (h \mathbf{u}) = 0, \quad (2)$$

where \mathbf{u} is the two-dimensional velocity field, h is the layer depth, f is the inertial frequency, g is the acceleration due to gravity, and \mathbf{k} is a unit vector perpendicular to the (x, y) -plane. The potential vorticity Q is given by $Q = (f + \mathbf{k} \cdot \nabla \times \mathbf{u})/h$. In general, f may be taken to be a function of latitude, but in this paper we shall take f to be constant.

In the present study the potential vorticity takes its uniform background value $Q_0 = f/h_0$ everywhere except in a strip of finite width Δ , where it takes a different value Q_1 . The potential vorticity jump is smoothed out over a small distance so that it can be represented in a finite-difference numerical scheme. The ratio of the difference between the strip and background potential vorticities, $Q_1 - Q_0$, to the background value, Q_0 , defines an effective Rossby number $Ro = Q_1/Q_0 - 1$ for the flow which, under this definition, may be either positive or negative. As the strip width is increased, so the velocities in the strip increase, and hence the Froude number $F = u/(gh_0)^{1/2}$ is governed by the width of the strip, and at small Froude number, F is a linear function of Δ . A small amount of dissipation at fine scales is also applied to the right-hand sides of (1) and (2) for numerical stability.

There are three significant reasons for choosing this type of initial flow.

(i) The initial flows are completely devoid of gravity waves, and hence all propagating gravity waves in the flow must be generated by vortical motions.

(ii) The vortical aspects of the flow are localized in the direction transverse to the initial shear flow, and there is a well-defined far field of gravity wave radiation distant from the vortical flow. The intensity of gravity wave radiation in this far field can then be taken as a measure of the strength of interaction between the vortical dynamics and the gravity waves in the system.

(iii) The parameter space is as simple as possible, with the Froude and Rossby numbers being controlled by two independent parameters of the initial flow: the width of the strip and the potential vorticity in the strip respectively.

All the flows simulated are unstable to the barotropic instability mechanism, described in terms of potential vorticity by Hoskins *et al.* (1985). An extensive review of shear flow instability was given by Ho & Huerre (1984). Although a study of the linear stability of a strip of potential vorticity in the shallow-water equations does not appear to have been published, the stability of a strip of potential vorticity in a class of balanced models, containing as limits of the class the two-dimensional Euler equations and the quasi-geostrophic equations, was recently studied by Waugh & Dritschel (1991). They found that, in the absence of externally imposed shear, the strip was always unstable to the barotropic shear flow instability mechanism, and in all cases the initial parallel flows described in this paper were readily found to be unstable. As

the instability develops, the potential vorticity rolls up into a train of vortices, spatially periodic in the streamwise direction. Many previous studies have addressed the subsequent merging of adjacent vortices as subharmonics of the fundamental wavelength of the primary instability develop (see Ho & Huerre (1984) and references therein). In this study, however, we are concerned with the degree to which the vortical motions, following the roll-up of the primary instability, will excite gravity waves which radiate away from the shear layer. To enable a thorough investigation of the Froude and Rossby number parameter space, numerical resources have been concentrated on simulating just one wavelength of the primary instability, with periodic boundary conditions in the streamwise direction of the period of the primary instability. It follows that subharmonics do not develop, and so the extent to which the vortex merging process excites gravity waves has not been investigated.

The rest of this paper is organized as follows. In §2 the Lighthill analysis for the shallow-water equations is developed, as appropriate for periodic jets. In §3 the pseudoenergy flux is introduced as an appropriate measure of gravity wave radiation, and its dependence on the Froude number is derived. In §4 the numerical model to be used for the nonlinear simulations is described, and an overview of the simulations performed with the model is presented in §5. In §6, the gravity wave radiation from a train of vortices generated by the roll-up of a cyclonic strip of potential vorticity is discussed. The strip has potential vorticity equal to six times the background value. In §7, the effect of increasing the potential vorticity in the strip is investigated. In §8, anticyclonic strips are investigated, with potential vorticity in the strips equal to 0.1 and 0 times the background value. In §9, the effect of negative potential vorticity is investigated, with potential vorticities in the strip of -0.1 , -1.0 and -19.0 times the background value. Some conclusions are offered in §10.

2. A ‘Lighthill’ theory of gravity wave generation for a periodic parallel flow

In this section the analysis necessary to investigate the quantitative accuracy of the Lighthill theory, applied to periodic flows in a rotating frame, is developed. In further sections the analysis will be used to investigate the degree to which the theory remains applicable as the Froude number is increased and the compact source assumption becomes less valid.

By an analysis similar to that presented by Lighthill (1952) for the compressible gas equations, manipulation of the shallow-water equations gives

$$\left(\frac{\partial^2}{\partial t^2} + f^2 - c_0^2 \nabla^2 \right) \frac{\partial h}{\partial t} = \frac{\partial^2}{\partial x_i \partial x_j} T_{ij}, \quad (3)$$

where
$$T_{ij} = \frac{\partial}{\partial t} (hu_i u_j) + \frac{1}{2} f (\epsilon_{ik} hu_j u_k + \epsilon_{jk} hu_i u_k) + \frac{1}{2} g \frac{\partial}{\partial t} (h - h_0)^2 \delta_{ij}, \quad (4)$$

h_0 is the layer depth far from the region of vortical motion, and $c_0 = (gh_0)^{1/2}$ is the gravity wave phase speed far from the region of vortical motion (see Ford *et al.* 1994). In (4), ϵ_{ij} is the two-dimensional antisymmetric tensor of rank two and unit determinant: $\epsilon_{11} = \epsilon_{22} = 0$; $\epsilon_{12} = -\epsilon_{21} = 1$. The left-hand side of (3) is simply the gravity wave operator acting on the time derivative of the height field, and the right-hand side is to be regarded as the effective source of gravity waves. The key point in Lighthill’s theory is now to assume that the source term T_{ij} is only non-zero over a

small enough region that the right-hand side of (3) may be approximated by a quadrupole point source, and further to assume that the source flow, and hence T_{ij} , may be regarded as known in terms of vortical dynamics, and can thus be computed without knowledge of the wave field. Both assumptions are valid in the limit of small Froude number, when the vortical flow is governed by the equations for a two-dimensional incompressible fluid, and the gravity wave wavelengths are $O(F^{-1})$ larger than the scale of the vortical flow (Crow 1970; Ford *et al.* 1994).

In comparing the gravity wave radiation with that predicted by the Lighthill theory, we shall concentrate on that component of the wave field which is independent of the streamwise coordinate x . In the asymptotic limit of small Froude number, it can be shown by the method of matched asymptotic expansions that all other components of the radiated wave field are exponentially small in Froude number compared with the x -independent component, and so this seems the natural component on which to focus the analysis.

Now, let the x -average of a quantity a be denoted by \bar{a}^x . To derive the effective source for the x -independent component of the wave field, we must take the x -average of (3). The x -derivatives, in both the wave operator and the quadrupole term, then vanish, and we are left with a one-dimensional Klein–Gordon equation, with a one-dimensional quadrupole source term:

$$\left(\frac{\partial^2}{\partial t^2} + f^2 - \frac{1}{c_0^2} \frac{\partial^2}{\partial y^2}\right) \frac{\partial \bar{h}^x}{\partial t} = \frac{\partial^2}{\partial y^2} \bar{T}_{22}^x. \quad (5)$$

To proceed, we need only assume that the source term \bar{T}_{22}^x is compact with respect to the cross-stream direction y . Making that assumption, we obtain

$$\frac{\partial \bar{h}^x}{\partial t}(y, t) = \frac{1}{2c_0} \frac{d^2}{dy^2} \int_{-\infty}^{t-|y|/c_0} S(t') J_0\{f[(t-t')^2 - y^2/c_0^2]^{1/2}\} dt', \quad (6)$$

where

$$S(t') = \int_{-\infty}^{\infty} \bar{T}_{22}^x(y', t') dy', \quad (7)$$

and J_0 is the regular Bessel function of order zero (see Morse & Feshbach 1953). The factor $\frac{1}{2}$ arises from the fact that waves propagate in both positive and negative y -directions away from the source at $y = 0$. To reconstruct the wave field from a numerical simulation using (6), we now need only know the function $S(t)$, a single function of time, which is obtained for each time t during the simulation by evaluating the integral (7) over the entire flow.

We may readily proceed from here to show how $\partial \bar{h}^x / \partial t$ in the wave region scales with properties of the vortical flow in the vortex train. Taking the Fourier transform of (5) with respect to t , making the compact source approximation, we have

$$i\omega \tilde{h} \sim \frac{(\omega^2 - f^2)^{1/2}}{2c_0} \exp[i(\omega^2 - f^2)^{1/2} y/c_0] \int \bar{T}_{22}^x(y', \omega) dy', \quad (8)$$

where, as usual, ω is the transform variable, and $\tilde{a}(\omega)$ is the Fourier transform of $a(t)$. Now, scale analysis of (4) gives a scaling for \bar{T}_{22}^x : $\bar{T}_{22}^x(y', \omega) \sim \omega \tilde{u}^2 h_0$, and hence, for $\omega^2 > f^2$,

$$h' \sim h_0 \left(\frac{u}{c_0}\right)^2 \left(\frac{(\omega^2 - f^2)^{1/2} \lambda}{c_0}\right), \quad (9)$$

where λ is the lengthscale of the vortical region.

3. A quantity to diagnose gravity radiation – the pseudoenergy flux

Since we are interested in the amplitude of gravity wave radiation over a wide range of Froude and Rossby numbers, it is desirable to take the flux of an appropriate wave quantity, such as pseudoenergy or pseudomomentum, as a measure of the strength of gravity wave radiation by the vortical flow.

In general, a wave activity density A is a field, second order in disturbance amplitude in the limit of small disturbances, for which there exists an associated wave flux F , such that

$$\frac{\partial A}{\partial t} + \nabla \cdot F = 0. \quad (10)$$

Definition of wave activities and their corresponding fluxes must be made with respect to some reference state. In this paper, we shall take the initial parallel flow as the reference state for the definition of wave activities and their fluxes. Throughout this section, \mathbf{u}_0 , h_0 and Q_0 represent the velocity, height and potential vorticity respectively of the basic state, and \mathbf{u}' and h' represent departures of velocity and height from the basic-state values. The basic state possesses symmetries with respect to x -translation and time translation, and therefore it is possible to define both pseudoenergy and x -pseudomomentum fluxes. For the present study, we are interested in developing a wave quantity which can be used to characterize the strength of gravity wave radiation. If we are to take a single quantity, such as a wave flux strength, to characterize gravity wave radiation, then that quantity should satisfy a monotonic radiation property – i.e. all radiating waves should give rise to fluxes of the same sign, at least in the limit of linear waves. It turns out that this ‘monotonic radiation property’ is not satisfied by the pseudomomentum, but is satisfied by the pseudoenergy (Ford 1993).

The technique for obtaining wave activities and fluxes is now quite well established (McIntyre & Shepherd 1987; Haynes 1988), and the details of the calculations of the pseudoenergy and pseudomomentum for the shallow-water equations will not be reproduced here. The pseudoenergy density is

$$A_e = \frac{1}{2}h(u'^2 + v'^2) + u_0 u' h' + \frac{1}{2}gh'^2 + h \int_{y_0}^y (Q - Q_0(y'))h_0(y')u_0(y') dy' \quad (11)$$

and its flux is

$$F_e = \mathbf{u}A_e + h_0 \mathbf{u}_0 \cdot \mathbf{u}' u' - \frac{1}{2}h_0 \mathbf{u}'^2 \mathbf{u}_0 + \frac{1}{2}gh'^2 \mathbf{u} + gh_0 h' u'. \quad (12)$$

In (11), y_0 is the initial y location of the fluid in the reference state which is at location (x, y) at the time t at which the wave activity density or flux is to be evaluated. The integral in (11) represents ‘Lagrangian information’ about the motion of fluid particles. Notice, however, that it will be non-zero only if the potential vorticity in the basic state is non-uniform between y and y_0 , implying that Rossby waves exist at the location y . In this paper, we shall be concerned with gravity wave fluxes in a region of uniform potential vorticity. In computing the fluxes far from the vortical region, therefore, the contribution to (11) from the potential vorticity integral will be identically zero, and Lagrangian information is therefore not required to evaluate F far from the vortical region.

It is then straightforward to show that the intensity of the pseudoenergy flux scales with the Froude number according to the expression

$$F_e \sim \begin{cases} h_0 c_0 F^4 \lambda^2 \omega (\omega^2 - f^2)^{1/2}, & \omega^2 > f^2 \\ 0, & \omega^2 < f^2. \end{cases} \quad (13)$$

Thus if, at low Froude numbers, we assume that the velocity u scales as $u \sim \omega\lambda$, and the Froude number $F \sim \omega\lambda/c_0$, it follows that

$$F_e \sim \begin{cases} h_0 c_0^3 F^6 (1 - f^2/\omega^2)^{1/2}, & \omega^2 > f^2 \\ 0, & \omega^2 < f^2. \end{cases} \quad (14)$$

Thus, if ω , c_0 and h_0 are held fixed, and the Froude number is increased by increasing λ , the scale of the vortical motions, the intensity of the pseudoenergy flux will increase as the sixth power of the Froude number, in agreement with the analysis of one-dimensional sound radiation by vortical motions presented by Ffowcs Williams (1969). However, if the Froude number is increased by increasing the magnitude of the vorticity in the vortical region, and therefore increasing $|\omega|$, no such simple scaling law applies. In general, for a given Froude number, the intensity of the wave fluxes will be greatest when $\omega^2 \gg f^2$, and the f^2/ω^2 term in (14) becomes insignificant.

4. The numerical model

The numerical model to be used integrates the nonlinear f -plane shallow-water equations in a channel geometry. The channel is periodic in the x -direction, and has solid boundaries at $y = \pm Y$, for some (usually large) Y . The shallow-water equations are integrated in non-dimensional form:

$$\frac{\partial \mathbf{u}}{\partial t} + \mathbf{u} \cdot \nabla \mathbf{u} + \mathbf{k} \times \mathbf{u} + \nabla h = \nu \frac{\partial^6 \mathbf{u}}{\partial x^6}, \quad (15)$$

$$\frac{\partial h}{\partial t} + \nabla \cdot (h\mathbf{u}) = \nu \frac{\partial^6 h}{\partial x^6}, \quad (16)$$

where \mathbf{u} is the two-dimensional velocity field, h is the layer depth, and \mathbf{k} is the unit vector normal to the plane. The non-dimensionalization sets the length scales and timescales for the flow, such that the unit timescale is the inertial period f^{-1} , and the unit lengthscale is the Rossby deformation radius $(gh_0)^{1/2}/f$. In (15) and (16), h has been rescaled so that g may be set to unity. The potential vorticity away from the region of vortical motions will therefore be unity. In subsequent sections, all results of model integrations will be presented using this non-dimensionalization of length- and timescales.

The model allows variable resolution in both the streamwise and cross-stream directions. The computational domain is periodic in x , but of finite extent in y , and the equations are discretized using finite differences in the y -direction, with fields at each value of y being represented as a sum of Fourier modes in x . The y -discretization is performed on a staggered grid, with u , v on physical grid levels, and h at intermediate levels. Streamwise derivatives are computed in spectral space, and nonlinear products computed in physical space. The variable cross-stream resolution was implemented using a coordinate transformation. The numerical model is written in terms of a cross-stream variable η . The grid positions are equally spaced in the model coordinate η , and the physical coordinate transformation is implemented by specifying a relationship between the model coordinate η and the physical coordinate y . Cross-stream differencing is performed on the η -grid, where centred differencing can be used. In the vortical region the value of $d\eta/dy$ is unity, whereas in the wave region its value is generally less than unity. In the region of variable resolution, a self-similar

transformation is employed, in which $d\eta/dy = e^{-a(\eta-\eta_1)}$, where η_1 is the outer limit of the region of high resolution, and a is a constant which sets the size of the region of variable cross-stream resolution. A maximum number of Fourier components is specified, which are to be used to represent the flow in the vortical region. Beginning at the start of the region of low cross-stream resolution, the number of Fourier components used to represent the solution is then reduced by a factor of two at every fifth cross-stream grid point, until a specified minimum number of streamwise components are left. This number of components is then used to represent the solution in the region of low resolution. In all simulations presented in this paper, 64 Fourier coefficients in the x -direction were used to resolve the vortical region.

Some diffusion is required to remove fine scales, especially in the vortical region. This was implemented by applying a small amount of hyperdiffusion to the Fourier components in each of the fields u , v and h . The hyperdiffusion is proportional to k^6 , where k is the wavenumber. The rotational nature of vortical flow renders it sufficient to apply a diffusion in the streamwise direction only. Any fine-scale structure which builds up in the cross-stream direction in the vortical flow rotates into a streamwise orientation, where it will be removed by the hyperdiffusion. This type of hyperdiffusion was used by Haynes (1989), and appears to control fine-scale structure adequately for the present purposes. Its advantage is that it is simple to implement, and may be implemented in an implicit diffusion scheme using only division, and not tridiagonal matrix inversion as would be required for isotropic diffusion with a grid-point discretization in the cross-stream direction. A general disadvantage of hyperdiffusion is that it tends to produce ‘Gibbs’ Fringes’. In particular, the potential vorticity on the edge of a vortex can, during the simulation, exceed the range of potential vorticity at the start of the simulation – something which is not possible with Laplacian diffusion (see, for example, the recent comparison of contour surgery and pseudo-spectral methods by Legras & Dritschel 1993). While Gibbs’ fringes may pose a serious problem for some numerical modelling applications, the comparison of the gravity wave radiation with the Lighthill theory in §§6–10 below shows that they should not be regarded as particularly detrimental for the purposes of the present study. Conservation of energy by the model was checked as the simulations proceeded, and typically the energy loss over the course of the simulations was less than 2%.

At the lateral boundaries, sponge layers may be placed in the model over a variable number of grid levels. Rayleigh friction is applied there, which relaxes the flow back to the initial state. The value of the Rayleigh friction is small at the point where it is first encountered by waves propagating towards the boundary, and increases linearly towards the boundary. For all simulations presented here, it was found that applying Rayleigh friction over 30 grid levels, with a maximum value of 1.0 at the boundary, corresponding to an e-folding decay time of 1.0 for disturbances at the boundary, generally prevented any noticeable reflection from the boundary, and these values were used throughout.

The equations are integrated forward in time using an explicit leapfrog time step, but with the hyperdiffusion and Rayleigh friction being performed implicitly. The basic leapfrog method is unstable, however, and a time filter must be used to prevent the growth of a rapidly oscillating computational mode. In the present simulations, a Robert–Asselin time filter (Robert 1966; Asselin 1972) was used with a value of 0.02.

		Initial strip width					
Simulation	$Ro \equiv Q_1 - 1$	i	ii	iii	iv	v	vi
A	5	0.018	0.035	0.07	0.14	0.21	0.28
B	8	0.018	0.035	0.07	0.21	—	—
C	20	0.011	0.021	0.041	0.081	—	—
D	-0.9	0.42	0.84	1.68	3.36	6.00	9.00
E	-1.0	0.42	0.84	1.26	2.52	6.00	—
F	-1.1	0.42	0.84	1.26	1.68	2.52	3.04
G	-2	0.07	0.21	0.42	0.63	—	—
H	-20	0.007	0.013	0.021	0.031	—	—

		Wavenumber of fastest growing mode					
Simulation	$Ro \equiv Q_1 - 1$	i	ii	iii	iv	v	vi
A	5	28.0	14.0	7.0	4.2	3.05	2.3
B	8	28.0	13.75	6.6	2.6	—	—
C	20	50.0	30.0	14.0	5.6	—	—
D	-0.9	2.0	1.15	0.75	0.475	0.245	0.165
E	-1.0	2.0	1.15	0.9	0.55	0.255	—
F	-1.1	2.0	1.15	0.9	0.75	0.55	0.47
G	-2	7.2	3.5	1.85	1.2	—	—
H	-20	65.0	44.0	30.0	20.0	—	—

		Froude number					
Simulation	$Ro \equiv Q_1 - 1$	i	ii	iii	iv	v	vi
A	5	0.11	0.20	0.36	0.50	0.59	0.66
B	8	0.17	0.32	0.53	0.84	—	—
C	20	0.23	0.37	0.66	1.06	—	—
D	-0.9	0.25	0.44	0.64	0.88	1.05	1.08
E	-1.0	0.30	0.51	0.64	0.99	1.78	—
F	-1.1	0.33	0.58	0.75	0.93	1.36	1.92
G	-2	0.17	0.38	0.73	1.31	—	—
H	-20	0.20	0.31	0.49	0.75	—	—

TABLE 1. Initial strip widths, fastest growing wavenumbers and Froude numbers for all simulations

5. Overview of numerical simulations

Using the numerical model described in §4, gravity wave generation by vortical motions in the shallow-water equations is now studied by numerical simulation of the nonlinear evolution of a barotropically unstable strip of potential vorticity. The potential vorticity in the strip is Q_1 , and the background value of the potential vorticity is unity. The Rossby number Ro can then be defined as $Ro = Q_1 - 1$. As discussed in the Introduction, the only other significant parameter in the initial flow is the width of the strip, Δ , which determines the Froude number of the flow.

In the following sections, simulations with a range of values of Q_1 and Δ are discussed. The simulations are labelled by letters A–H, with each letter corresponding to a different value of Q_1 . Simulations with the same value of Q_1 are distinguished by Roman numerals (e.g. Ai–vi), with the Roman numeral increasing with increasing initial strip width. Table 1(a) shows the values of Q_1 and Δ investigated, with their corresponding labels.

In all cases, the initial conditions for the numerical simulation consist of a strip of

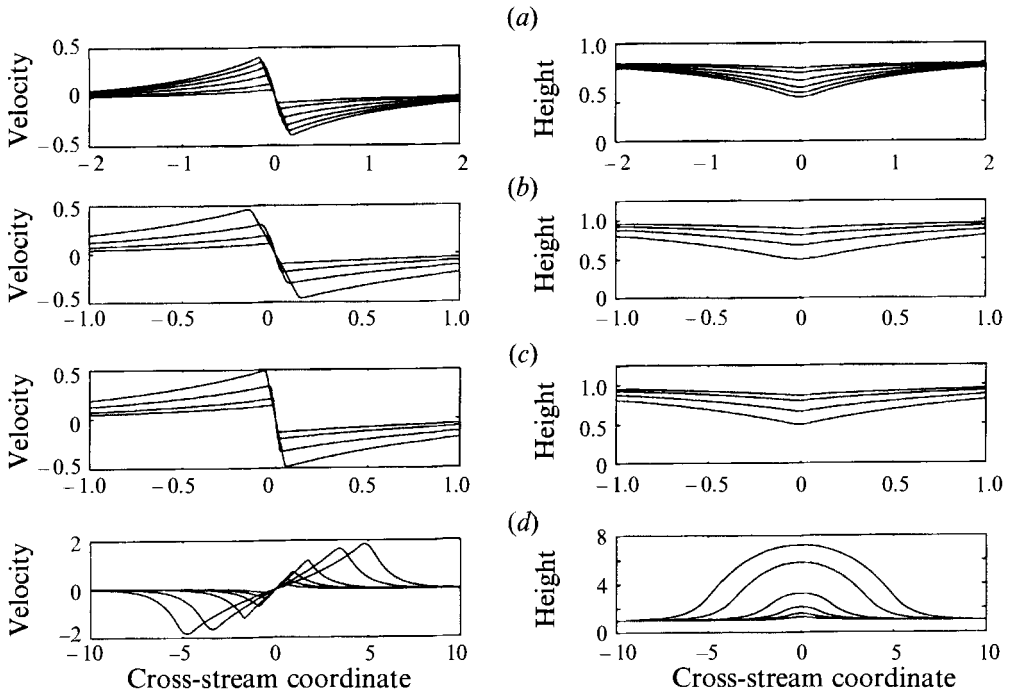


FIGURE 1. Jet velocity and height fields for the initial states: strip potential vorticity positive. (a) $Q = 6$, (b) $Q = 9$, (c) $Q = 21$, (d) $Q = 0.1$.

potential vorticity Q_1 centred on $y = 0$. The initial velocity and height fields for all simulations are shown in figures 1 and 2. Figure 1 shows the cases with positive potential vorticity in the strip, whereas figure 2 shows the cases with zero or negative potential vorticity in the strip. In all cases, the initial flow consists of two jets, flowing in opposite directions, with one jet centred at $y = +\frac{1}{2}\Delta$, and the other centred at $y = -\frac{1}{2}\Delta$. For positive potential vorticity in the strip, the gradient of the jet velocity decreases as the strip width increases, whereas for zero or negative potential vorticity in the strip, the gradient of the jet velocity increases as the strip width increases. The corresponding height fields are depressions for cyclonic potential vorticity, and elevations for anticyclonic potential vorticity.

The model domain in the cross-stream direction extends from $y = -Y$ to $+Y$, for some large Y (see table 2), to accommodate several wavelengths of the radiating gravity waves within the computational domain. Only one wavelength of the fastest growing unstable linear eigenmode is simulated in all cases. The wavenumber of the fastest growing eigenmode is shown in table 1(b), and a matrix method is used to obtain the eigenmode. In all cases except simulations Ci-iv and Hi-iv, a small-amplitude disturbance of the form of the fastest growing eigenmode is added to the initial parallel flow at $t = 0$. If a large amplitude of the fastest growing eigenmode is added, then the flow will adjust, radiating gravity waves. The amplitude of the eigenmode added was therefore controlled such that any gravity waves generated by this initial adjustment had an amplitude of no more than 1–2% of the gravity waves subsequently by the vortical motions, when viewed in the $\partial h/\partial t$ field. In cases Ci-iv and Hi-iv, the strips are very narrow compared with a deformation radius. Consequently, the eigenmode decays very slowly with distance away from the strip, when compared with the width of the strip. This presents very large memory requirements for the matrix method used

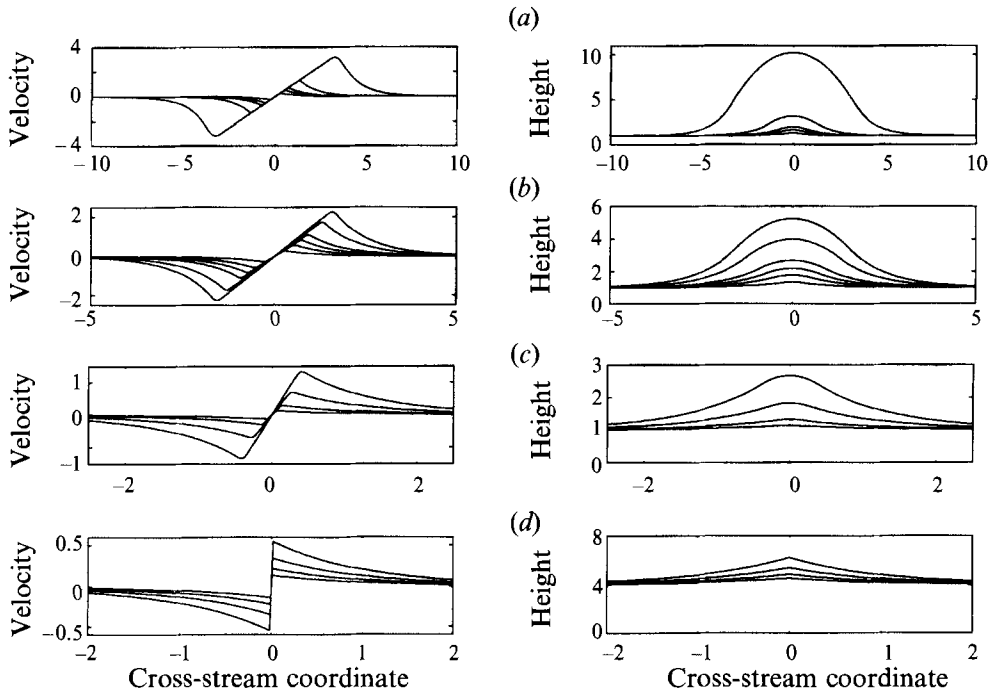


FIGURE 2. Jet velocity and height fields for the initial states: strip potential vorticity zero and negative. (a) $Q = 0$, (b) $Q = -0.1$, (c) $Q = -1$, (d) $Q = 19$.

to find the eigenmode, and in these cases the flow was disturbed by the addition of random noise. Again, the amplitude of the random noise added was chosen to be sufficiently small that any gravity wave radiation associated with it was of small amplitude compared with the gravity waves subsequently generated by the vortical motions.

In the nonlinear evolution of the flow, the strip of potential vorticity rolls up into a train of vortices, which then nutate, radiating gravity waves as they do so. In general, it was found that the maximum value of the Froude number throughout the fluid, which is found in the vortical region, can increase by as much as 50% during the initial development of the instability, and then tends to fluctuate as the vortices nutate. In subsequent sections, we shall consider how the amplitude of the flux of the radiated gravity waves scale with the Froude number, with reference to the predictions made in §§2 and 3, and in particular equation (14). Therefore, as a measure of the Froude number of the flow, we shall require a Froude number associated with the gravity wave generation phase of the flow, rather than the initial roll-up phase. For this reason, the maximum value of the Froude number over all times was taken to characterize the Froude number of the flow, and for each simulation this value is shown in table 1(c).

With the values of Q_1 and Δ selected, the remaining parameter which must be adjusted is the hyperdiffusion. Since it has no physical meaning, it was selected by experimentation with the simulation Aiii, with the aim of finding the minimum value which presented an unacceptable build-up of noise on small scales in the potential vorticity field. On the other hand, it was important to ensure that the vortices did not become axisymmetric too quickly as a result of excessive hyperdiffusion, and therefore lose their ability to radiate gravity waves. It was found that 64 Fourier coefficients were required to represent the fields at each cross-stream grid level if the required level of

	Simulation	$(\Delta y)^i$	Ny^i	$(\Delta y)^e$	Ny^e	Y	Nx^e	Δt
A	i	0.0025	150	0.0625	1000	24.5	8	0.000625
	ii	0.005	150	0.125	600	24.1	8	0.00125
	iii	0.01	350	0.2	1000	59.8	8	0.0025
	iv	0.01	350	0.2	1000	59.8	8	0.0025
	v	0.01	350	0.2	1000	59.8	8	0.0025
	vi	0.01	350	0.2	1000	59.8	8	0.0025
B	i	0.0025	150	0.0625	1000	24.5	8	0.000625
	ii	0.005	150	0.125	600	24.1	8	0.00125
	iii	0.01	350	0.2	1000	59.8	8	0.0025
	iv	0.01	350	0.2	1000	59.8	8	0.0025
C	i	0.001	350	0.02	1000	5.98	8	0.00025
	ii	0.001	350	0.02	1000	5.98	8	0.00025
	iii	0.001	350	0.02	1000	5.98	8	0.00025
	iv	0.004	350	0.04	1000	12.5	16	0.001
D	i	0.02	350	0.2	1000	62.3	8	0.005
	ii	0.04	350	0.2	1000	66.9	8	0.01
	iii	0.04	350	0.2	1000	66.9	16	0.01
	iv	0.04	500	0.2	1000	54.9	16	0.005
	v	0.2	600	0.2	600	59.9	64	0.025
	vi	0.2	600	0.2	600	59.9	64	0.025
E	i	0.02	350	0.2	1000	62.3	8	0.005
	ii	0.04	350	0.2	1000	66.9	8	0.01
	iii	0.04	350	0.2	1000	66.9	16	0.01
	iv	0.04	425	0.2	1000	61.0	16	0.005
	v	0.2	600	0.2	600	40.0	64	0.0125
F	i	0.02	350	0.2	1000	62.3	8	0.005
	ii	0.04	350	0.2	1000	66.9	8	0.01
	iii	0.04	350	0.2	1000	66.9	16	0.01
	iv	0.04	350	0.2	1000	66.9	16	0.005
	v	0.04	2000	0.04	2000	40.0	64	0.005
	vi	0.04	1000	0.04	1000	20.0	64	0.0025
G	i	0.01	350	0.2	1000	59.8	8	0.0025
	ii	0.01	350	0.2	1000	59.8	8	0.0025
	iii	0.02	350	0.2	1000	62.3	8	0.005
	iv	0.03	2000	0.03	2000	30.0	64	0.005
H	i	0.001	350	0.025	1000	9.81	8	0.00025
	ii	0.001	350	0.02	1000	5.98	8	0.00025
	iii	0.001	350	0.02	1000	5.98	8	0.00025
	iv	0.001	350	0.02	1000	5.98	16	0.000125

TABLE 2. Details of numerical resolution used in all experiments. $(\Delta y)^i$ is the cross-stream grid spacing in the vortical region; Ny^i is the number of cross-stream gridpoints in the vortical region; $(\Delta y)^e$ is the cross-stream grid spacing in the wave region; Ny^e is the total number of cross-stream gridpoints; Y is the distance of the boundary from the centre of the domain in the cross-stream direction; Nx^e is the number of Fourier coefficients in the streamwise direction used to resolve the wave region; Δt is the timestep

hyperdiffusion was not to be so great as to cause the vortices to become axisymmetric after one or two nutations. With the value of the hyperdiffusion ν selected, it was then adjusted between simulations so as keep $\nu k_{max}^6 \times (\delta Q)$ constant, where k_{max} is the maximum wavenumber in the simulation, and (δQ) is the magnitude of the potential vorticity difference between the vortices and the surroundings, meaning that in all

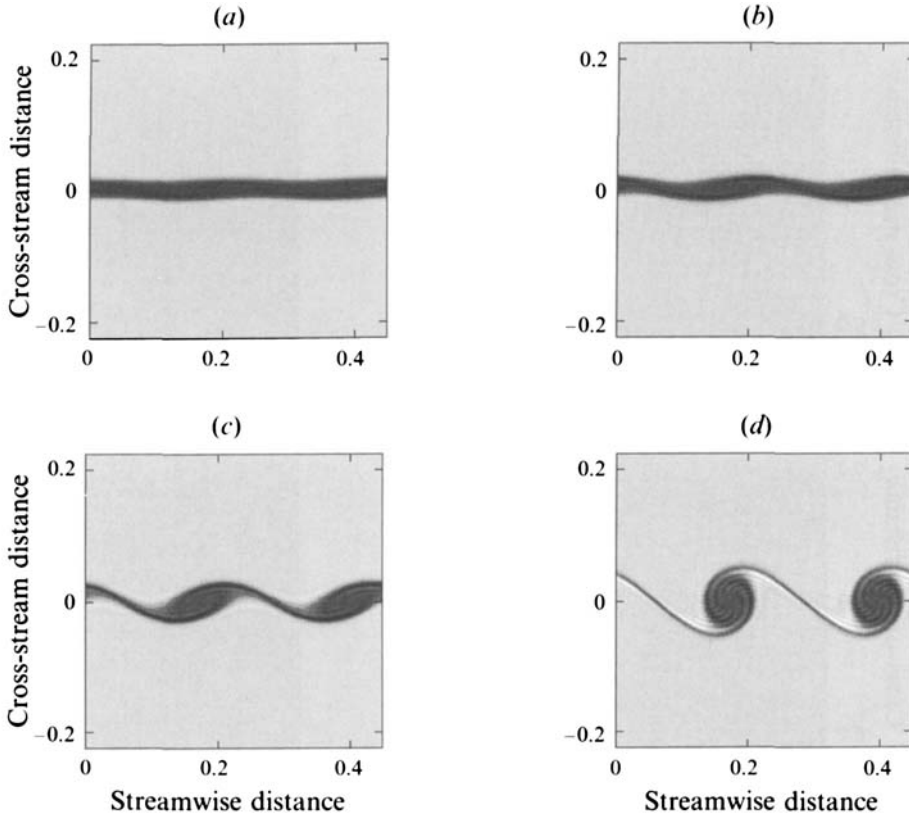


FIGURE 3. Early stages of vortical evolution, simulation Ai: (a), (b), (c), (d) correspond to times 1.56, 2.81, 4.06 and 5.31 respectively. Two periods of the model domain are shown.

simulations it takes the same amount of time to damp out noise in the highest wavenumbers, based on typical vortex dynamical timescales set by the magnitude of the potential vorticity variations. For $k = 1.0$ and $(\delta Q) = 1.0$, the value of ν used is $\nu = 6.4 \times 10^{-9}$.

To accommodate the wide range of strip widths (see table 1 a), the grid-point spacing in the cross-stream direction had to be changed between simulations. In all cases, the region of uniform potential vorticity in the strip was distributed over at least seven grid intervals, and the potential vorticity was adjusted to the background value over five grid intervals. Details of the cross-stream resolution for all simulations are given in table 2. For the streamwise resolution, the 64 Fourier coefficients which were used in the vortical region were frequently more than sufficient to resolve the flow in the wave region. Therefore, in addition to varying the cross-stream resolution, the streamwise resolution was also varied, as described in §4. The number of Fourier coefficients used in the wave region are given in table 2.

6. Jets with moderate Rossby number and variable Froude number

In the first set of numerical experiments, to be described in this section, the Rossby number is fixed, and the effect of varying the Froude number is investigated. In all these cases, therefore, the model is initialized with a strip in which the potential vorticity is

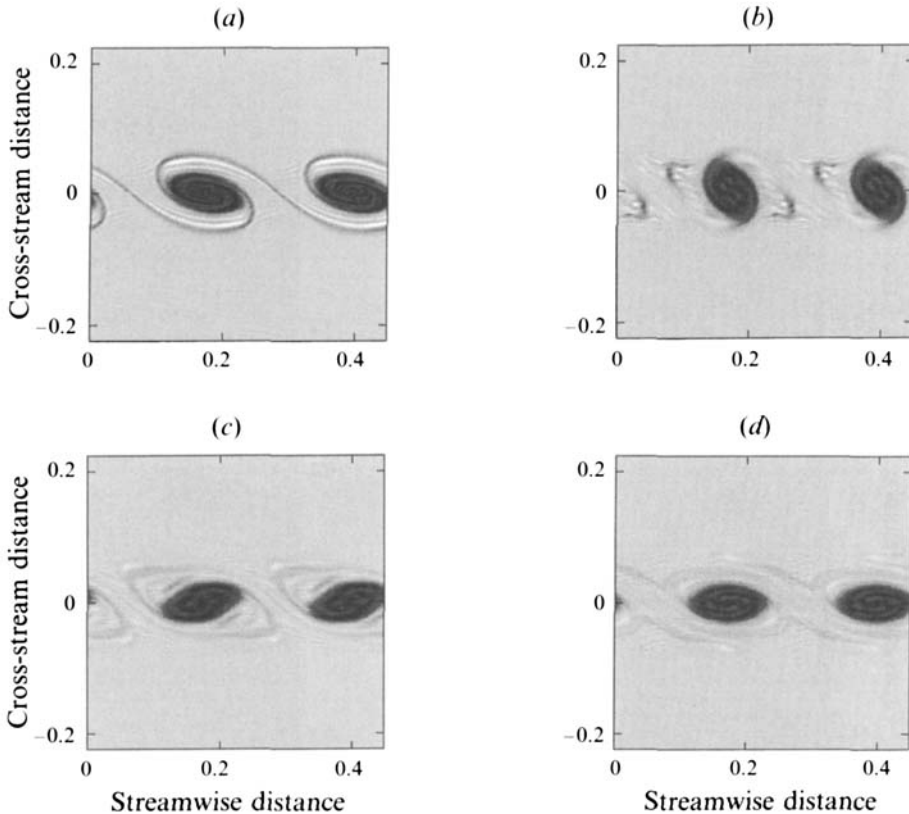


FIGURE 4. Nonlinear evolution of potential vorticity field, simulation A i: (a), (b), (c), (d) correspond to times 6.56, 12.2, 17.8 and 23.4 respectively. Two periods of the model domain are shown.

equal to six times the background value. This can be regarded as fixing the Rossby number at 5. The Froude number then is varied by varying the width of the strip.

Six simulations were performed with the potential vorticity in the strip equal to six times the background value. Initial strip widths of 0.018, 0.035, 0.07, 0.14, 0.21 and 0.28 were used. The corresponding Froude numbers found in the subsequent evolution varied from 0.11 to 0.67, increasing monotonically as the initial strip width increased.

Figure 3 shows the potential vorticity field during the initial development and saturation of the instability in the simulation A i. All potential vorticity plots are shown with an aspect ratio of unity, and consequently they show only a small portion of the domain in the cross-stream direction. While the model domain accommodates only one wavelength of the primary instability in the streamwise direction, in this, and all subsequent figures shown, two periods of the model domain are displayed. One can see that, as the instability develops, waves develop on the edges of the potential vorticity strip, which can be seen clearly in figures 3(b) and 3(c). Nonlinear saturation of the instability is shown in figure 3(d), where the strip has rolled up into a train of coherent vortices, connected by thin filaments.

Figure 4 shows the potential vorticity field at four subsequent equally spaced time intervals until the end of the simulation. Although a small amount of hyperdiffusion is applied in the x -direction to prevent an accumulation of noise on the grid scale of the numerical model, it seems that the inviscid character of the vortical flow has been well simulated in this experiment. The vortices appear to nutate between almost

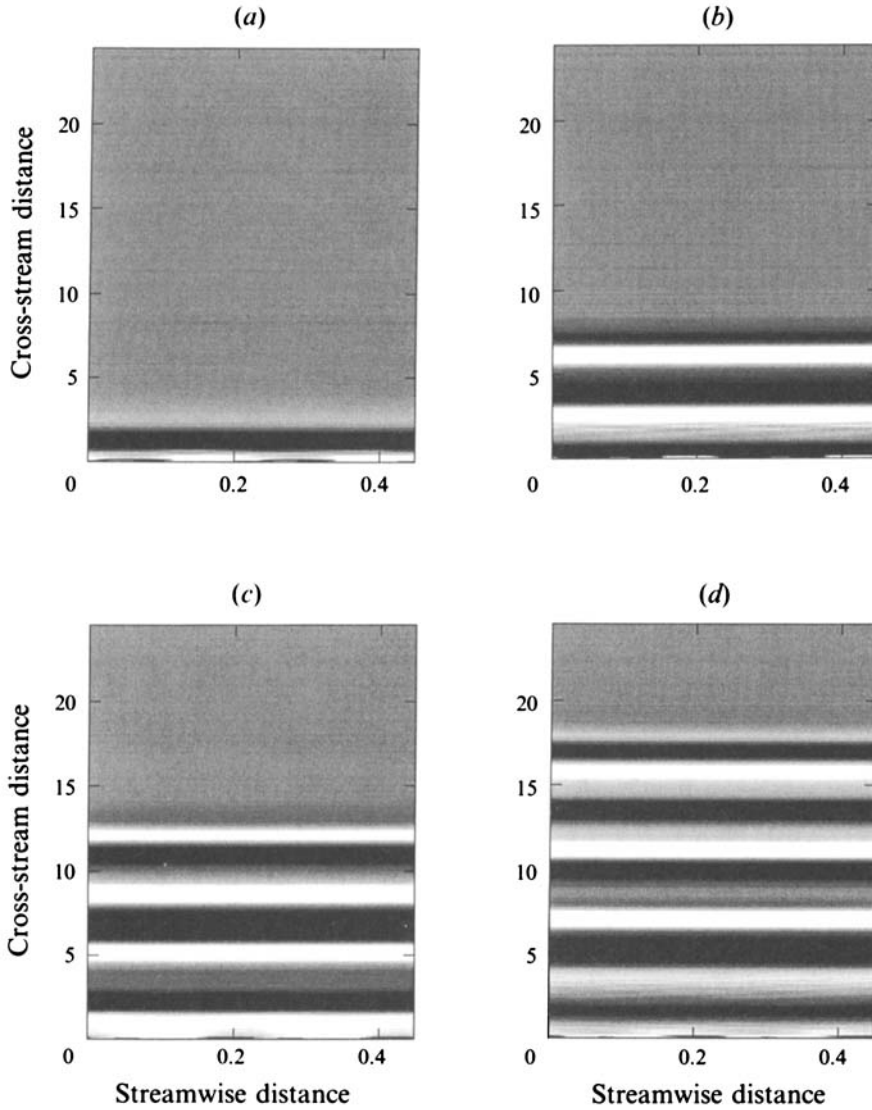


FIGURE 5. Development of gravity wave radiation, simulation A1: (a), (b), (c), (d) correspond to times 6.56, 12.2, 17.8 and 23.4 respectively. Two periods of the model domain are shown.

axisymmetric and substantially elliptical shapes, whereas if the hyperdiffusion is increased significantly they become axisymmetric after only two or three nutations. This behaviour has also been observed by Lele & Ho (1994), and can be seen in the incompressible simulations of Pozrikidis & Higdon (1985, see especially their figure 6).

Linear gravity waves have zero potential vorticity perturbation, and so they are not observed in the potential vorticity plots shown in figures 3 and 4. However, we recall from (5) that, in the absence of nonlinearity, the Eulerian time derivative of the height field, $\partial h/\partial t$, satisfies the linear wave equation for gravity waves, i.e.

$$\left(\frac{\partial^2}{\partial t^2} + f^2 - c_0^2 \nabla^2\right) \frac{\partial h}{\partial t} = \text{nonlinear terms.} \quad (17)$$

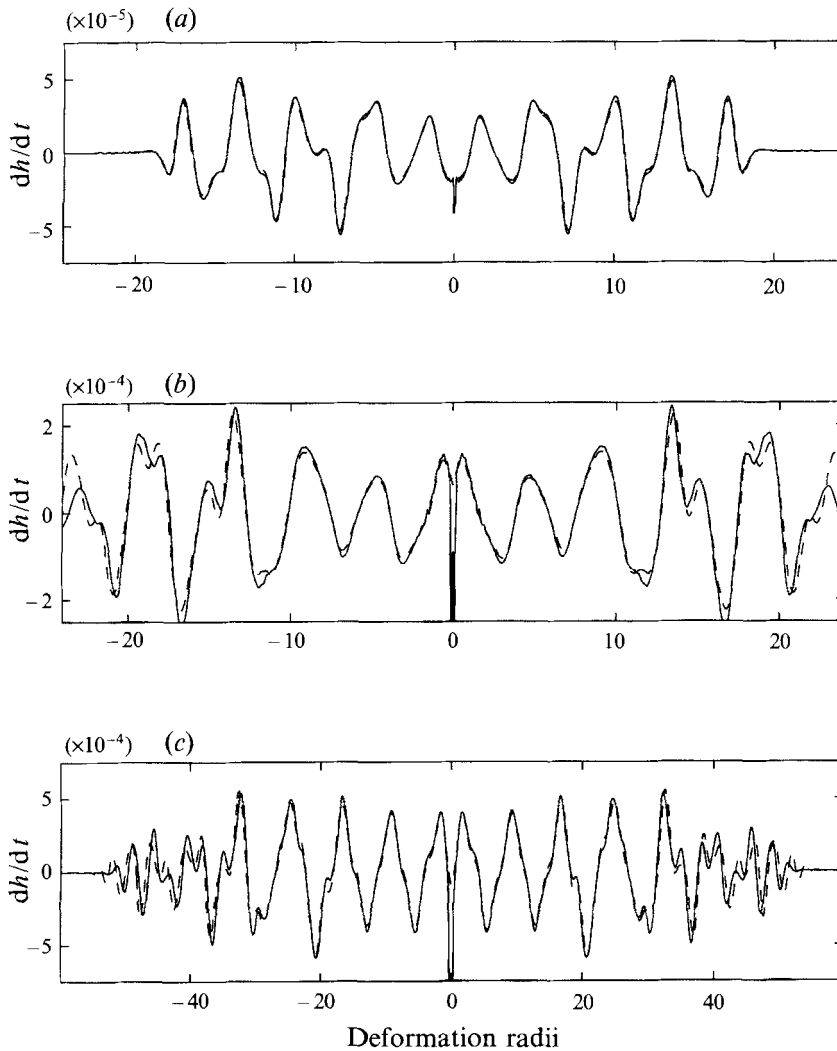


FIGURE 6. The x -averaged $\partial h/\partial t$ field at the termination of simulations (a) Ai, (b) Aii, (c) Aiii. Solid lines are from the nonlinear simulation, and dashed lines are from the Lighthill convolution integral.

It is therefore natural to use $\partial h/\partial t$ to investigate gravity waves radiated by the shear instability. For each of the times shown in figure 4, the corresponding $\partial h/\partial t$ field is shown in figure 5. Only the region $y > 0$ is shown, since all simulations are symmetric about $y = 0$. The entire computational domain for $y > 0$ is shown in all plots of $\partial h/\partial t$, and in figure 5 this requires that the cross-stream direction be compressed compared with the streamwise direction. As in the case of the potential vorticity field, two periods of the model domain in the streamwise direction are shown in all plots of $\partial h/\partial t$. The greyscale map is chosen to saturate at the peak amplitudes in the wave region, even though typical values of $\partial h/\partial t$ in the vortical region may be more than ten times greater than those found in the wave region. No quantitative information should be inferred from the greyscale plots of $\partial h/\partial t$ shown in this paper. We shall address the quantitative aspects of the gravity wave radiation when we compare the waves generated with those predicted by the Lighthill theory, and discuss the way in which the amplitude of the radiating wave fluxes depend on the Froude and Rossby numbers of the vortical flow.

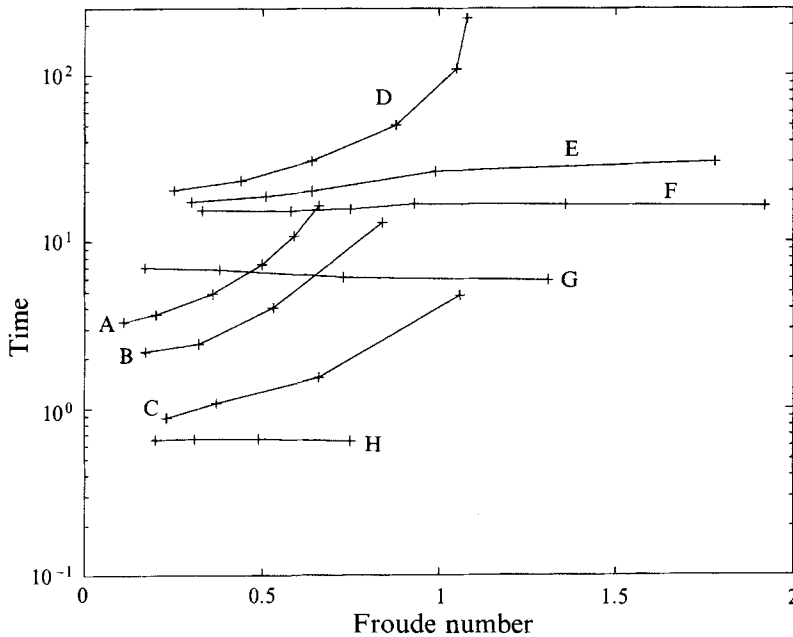


FIGURE 7. Vortex nutation times for all experiments, A–H.

In the greyscale figure 5, however, two features of the radiated gravity wave field are nonetheless particularly striking. Firstly, the wavelength of the gravity waves is much longer than the cross-stream scale of the vortical motions. Secondly, the radiated gravity wave field is almost independent of the streamwise coordinate x . This means that we should expect the reconstruction of the gravity wave field from the Lighthill source term to be quite good for this simulation.

In figure 6, the x -averaged $\partial h/\partial t$ field is shown at the termination of simulations A i–iii. The solid lines in figure 6 are the x -average of the height field obtained directly from the nonlinear simulation. The dashed lines are the result of using the source term $S(t)$, obtained from (7), in the convolution integral (6), and are therefore the wave field predicted by this modified form of the Lighthill theory. For simulation A i, the agreement between the full simulation and the Lighthill reconstruction seems very good. This is reassuring, partly because the Froude number is quite small, and the compact source approximation should be reasonably accurate for this flow, and partly because it means that the numerical model is performing sufficiently well to capture the Lighthill mechanism, and that the resolution employed is adequate to reconstruct the Lighthill source term for the convolution integral (6).

As the initial strip width is increased, visual inspection of the potential vorticity field (not shown) indicates little difference in the vortical aspects of the dynamics between each of the three simulations A i–iii. In each case, the strip of high potential vorticity rolls up into a periodic train of vortices, which subsequently nutate. However, there is a perceptible difference in the nutation times for the vortices. The nutation times for vortices in all simulations A–H are shown in figure 7, which shows that, for simulations A i–iii, the nutation time for the vortices increases from 3.44 inertial periods (simulation A i) to 4.88 inertial periods (simulation A iii). The vortex nutation times are a significant feature of the flow, in that they are a broad measure of the degree of unsteadiness of the vortical flow compared with the unit inertial period.

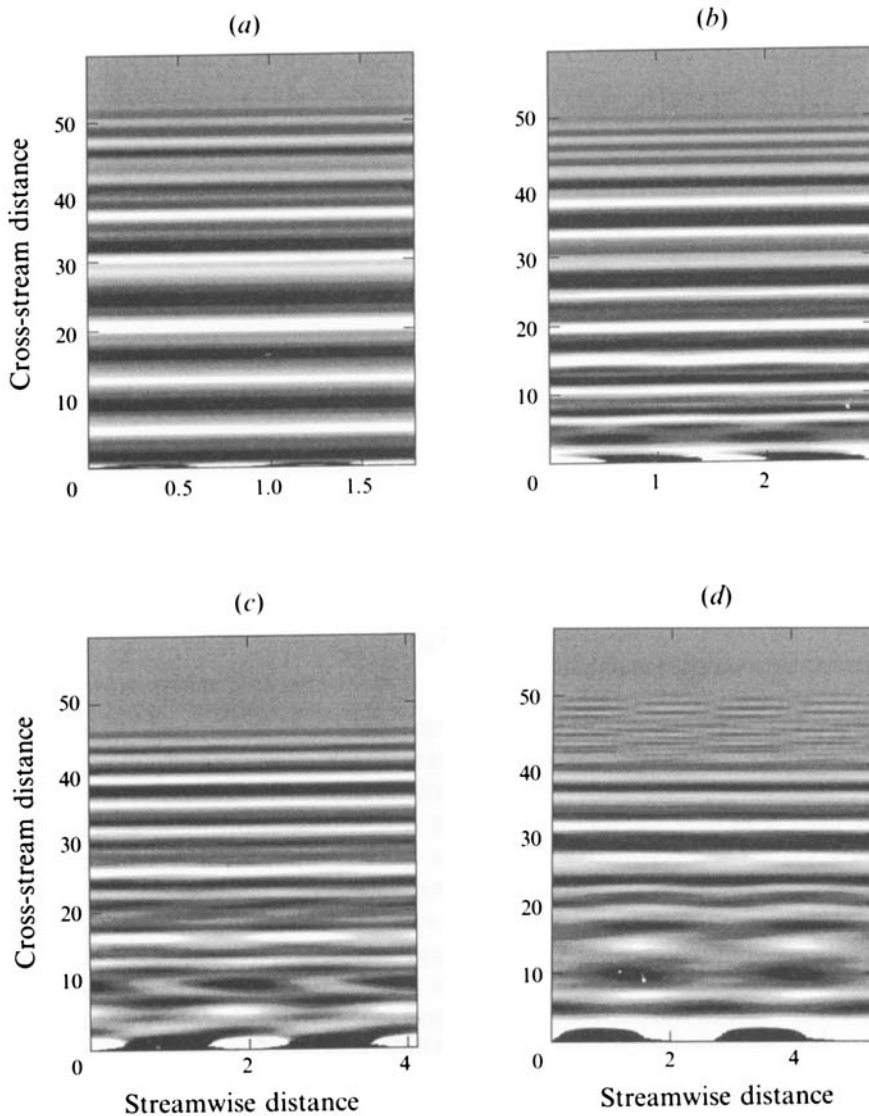


FIGURE 8. The $\partial h/\partial t$ field at the termination of simulations Aiii–vi (*a–d* respectively) (time 62.5). Two periods of the model domain are shown.

Considering now the gravity wave aspects of flows Aii and Aiii, the form of the radiated gravity waves remains similar in these two cases to those observed in simulation Ai. In figure 6, one can see that the agreement between the simulated wave field and its reconstruction from the Lighthill source term is quite good in each case. From figure 6, we can also see that the amplitude of the radiated gravity waves increases by a factor of about 12 between Ai and Aiii. The maximum Froude number found during the evolution increases from 0.11 (Ai) to 0.36 (Aiii) (see table 1*c*), and we recall from (9) that, as the Froude number is increased, we expect the amplitude of the radiated gravity waves to increase as the third power of the Froude number. Thus, on the basis of the low-Froude-number asymptotic analysis, we should expect the gravity wave amplitude to change by a factor of 35. Evidently, the increase in gravity

wave amplitude as a function of Froude number over this range is not quite as large as one might expect on the basis of the Lighthill theory. Two assumptions were made to predict that the amplitude of the radiated waves would scale with the third power of the Froude number: the point source assumption, and the scaling assumption $u \sim \omega l$. The fact that the wave amplitudes do not increase as rapidly as the theory predicts is thus not necessarily an indication that the point source approximation will fail for these simulations, and could be attributable to the breakdown of the scaling assumption $u \sim \omega l$, which is consistent with the observation of increasing nutation times.

Three further simulations (Aiv–vi) were then performed, with strip widths of 0.14, 0.21, and 0.28. The vortical aspects of the flow remained qualitatively unchanged as the width of the strip, and hence the Froude number, was increased. In each case, the strip initially rolled up into a periodic train of vortices, which were allowed to rotate several times before the simulation was terminated. The most significant quantitative difference in the vortical aspects of the flow between these three cases is in the nutation rate of the vortices in the train, shown in figure 7, which increase apparently super-exponentially with increasing Froude number.

Figure 8 shows the $\partial h / \partial t$ field at the termination of the simulations Aiii–vi. The main point is that, as the Froude number is increased, the radiated gravity waves develop more x -dependent structure. The gravity wave field is expected to be x -independent at low Froude numbers, and it is reasonable to expect more x -dependence in the field as the Froude number is increased, and the lengthscale separation between the vortices and the gravity waves diminishes.

Figure 9 shows the x -averaged $\partial h / \partial t$ field at the termination of simulations Aiii–vi, and its reconstruction from the Lighthill source term. The most striking feature of the sequence of figures is that, in contrast to the rapid increase in wave amplitude with Froude number predicted by Lighthill's scaling argument, the radiated wave amplitudes actually decrease. This clearly differs from the scaling arguments presented by numerous authors on aeroacoustics, which were discussed in §§2 and 3, and from the mass of experimental data that confirm the Lighthill scaling in practice (Moore 1977).

Since the only new effect in the present study is the inclusion of background rotation, it follows that background rotation must be responsible for decreasing the wave amplitude as the Froude number is increased. Moreover, since the reconstruction of the wave field from the Lighthill source term effectively captures the decrease in wave amplitude, it must be explicable within the framework of the Lighthill theory.

There are two possibilities. One is that the quadrupole source strength decreases, rather than increases, as the Froude number is increased. However, we should bear in mind that in order for the quadrupole source to excite propagating waves, it must have a significant component of its frequency above the inertial frequency. Therefore, a second possibility is that, although the magnitude of the source terms might actually increase as the Froude number is increased, their frequency component above the inertial frequency might decrease.

Figure 10 shows the integrated source term $S(t)$ for each of the simulations Ai–vi as a function of time. In general, the amplitude of the source term increases with increasing Froude number, but with frequency decreasing very rapidly with increasing Froude number. It seems, therefore, that the effect of the inertial cut-off, inhibiting gravity wave radiation at frequencies below the inertial frequency, is now dominant over the increased magnitude of the source term, leading to reduced wave amplitudes as the Froude number is further increased.

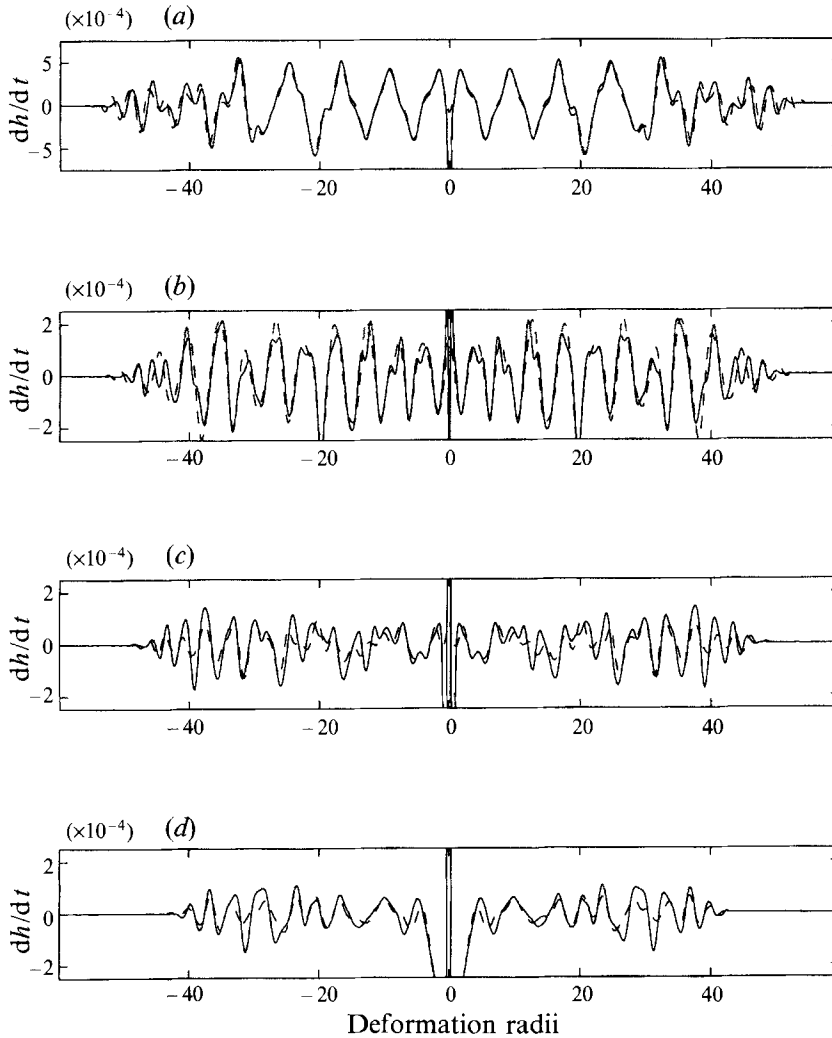


FIGURE 9. The x -averaged $\partial h/\partial t$ field at the end of simulations Aiii–vi (a – d respectively).

We may conclude that, although the potential vorticity in the strip was chosen to be six times the background value, both the vortical flow and the wave generation process are significantly affected by the presence of background rotation. For small Froude numbers (between 0.11 and 0.35), the amplitude of the radiated gravity waves increases with Froude number, although not quite as rapidly as F^3 , as found in the asymptotic limit $F \ll 1$. When the Froude number exceeds 0.35, however, the radiated gravity wave amplitudes are found to decrease with increasing Froude number, even though the typical amplitudes of $S(t)$ are generally increasing. This behaviour has never been found in numerical or laboratory experiments in a non-rotating frame. The presence of background rotation thus severely inhibits gravity wave radiation at moderate Rossby numbers, and there seems little doubt that the present study has investigated a case in which the effect of background rotation is quite strong, despite a notional Rossby number of 5. Therefore, in the next section, we investigate the effect of increasing the potential vorticity in the strip. The strip remains cyclonic, but the effect of background rotation should decrease as the potential vorticity in the strip increases.

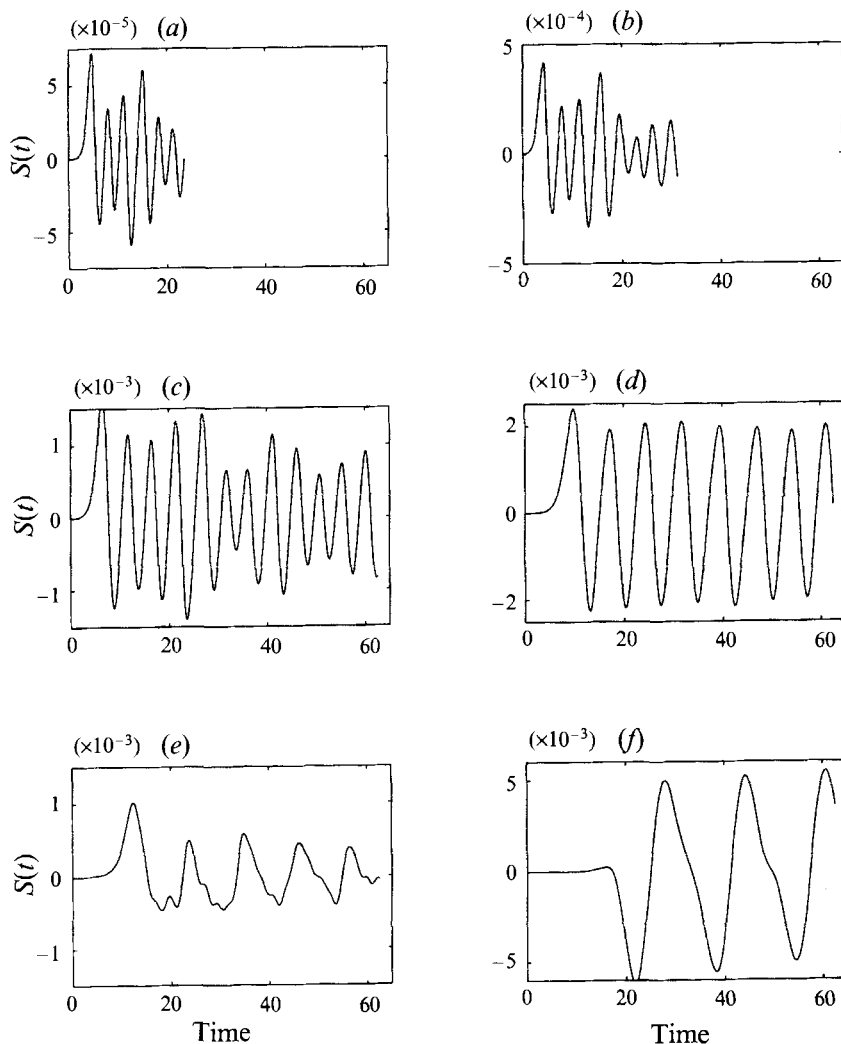


FIGURE 10. The source term $S(t)$ for simulations Ai–vi (a – f respectively). Note the differing scales on the $S(t)$ axes.

7. Cyclonic strips at large Rossby number

In this section the results of simulations with strip potential vorticities of 9 and 21 are presented. There are four simulations with strip potential vorticity 9, labelled Bi–iv, and four with strip potential vorticity of 21, labelled Ci–iv. In neither set of simulations should we expect to observe any qualitative difference from the simulations with potential vorticity of 6 in the strip. Quantitatively, we should expect to see more rapid vortical motions, and consequently a larger pseudoenergy flux in the radiated wave field.

In simulations Bi–iv, the initial step widths are 0.018, 0.035, 0.07 and 0.21, resulting in Froude numbers of 0.17, 0.32, 0.53 and 0.84 respectively. In each case, the strip rolls up into a periodic train of vortices, which then nutate, radiating gravity waves. The vortical flow appears very similar to that observed in experiments Ai–vi, and potential vorticity plots are not shown here. The nutation periods for these vortices are shorter than for the corresponding simulations in sequence A, but still appear to increase

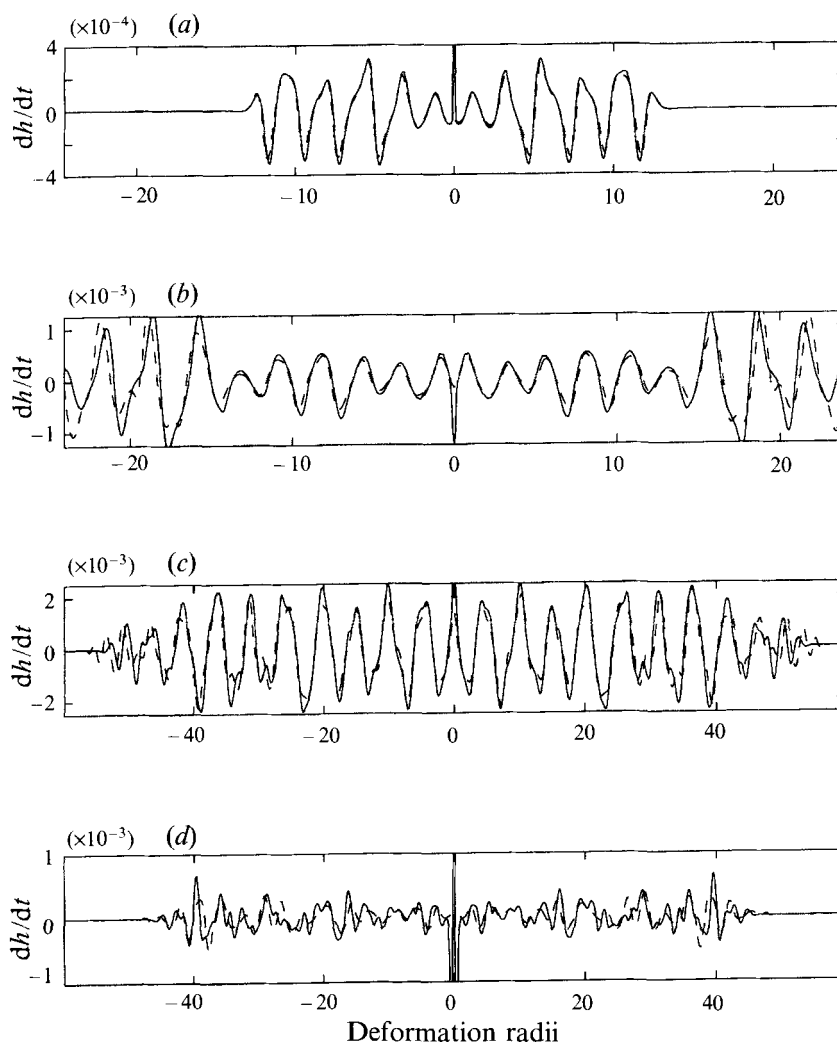


FIGURE 11. The x -averaged $\partial h/\partial t$ field at the termination of simulations Bi–iv (*a–d* respectively). Solid lines are from the nonlinear simulation, and dashed lines are from the Lighthill convolution integral.

super-exponentially with increasing Froude number (figure 7), in common with sequence A. The $\partial h/\partial t$ field follows broadly the same pattern as in the lower Rossby number simulations Ai–vi. At small Froude numbers, the wave field is almost independent of x , and as the Froude number is increased, amplitudes of the x -dependent modes increase.

In figure 11, the x -averaged wave field is shown at the end of each simulation (solid line), and compared with its reconstruction from the Lighthill theory (dashed line). Overall, there is good agreement between the Lighthill theory and the numerical simulations, as there was in the lower-Rossby-number simulations Ai–vi. As before, the agreement is best when the Froude number is lowest. The radiated wave amplitudes are seen to increase with increasing Froude number for simulations Bi–iii, but then decrease between Biii and Biv.

The maximum pseudoenergy flux in the radiated wave field for simulations A–H is shown in figure 12. The dashed line is a line of gradient 6 on the log–log scale, which

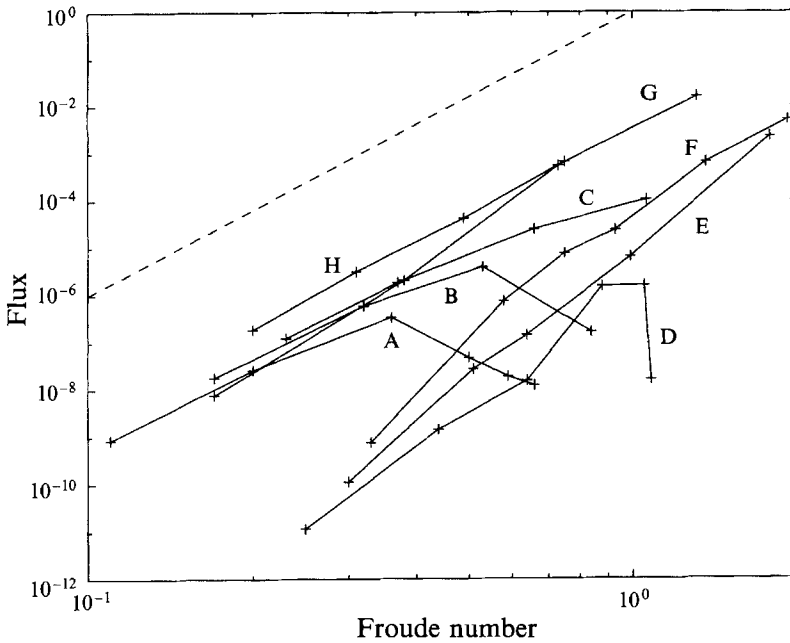


FIGURE 12. Pseudoenergy flux against Froude number for all simulations (solid lines). The gradient of the dashed line corresponds to pseudoenergy increasing as the sixth power of the Froude number.

is the gradient predicted by the small-Froude-number asymptotics (equation (14)). The Froude number at which the maximum pseudoenergy flux occurs is greater in case B than in case A, but the strip width at which the transition from increasing to decreasing pseudoenergy fluxes appears to be about the same, at around 0.1.

Overall, increasing the potential vorticity in the strip from 6 to 9 has the effect of increasing the amplitude of radiated gravity waves, and their corresponding pseudoenergy fluxes. However, in both cases, there exists a Froude number (or equivalently a strip width) which is in some sense optimal for gravity wave radiation. The amplitude of the x -averaged pseudoenergy flux of radiated gravity waves increases with increasing Froude number up to this critical Froude number, but then decreases as the Froude number is increased further.

Four further experiments, Ci–iv, were then performed with a strip potential vorticity of 21. These correspond to initial strip widths of 0.011, 0.021, 0.041 and 0.081 respectively. Once again, in each case the strip rolls up into a periodic train of vortices, which then nutate several times before the simulation is terminated. The dependence of the nutation time upon the Froude number, shown in figure 7, is consistent with the behaviour found in experiments A and B, i.e. it appears to be increasing super-exponentially with Froude number.

The comparison of the x -averaged $\partial h/\partial t$ field with its reconstruction by the Lighthill theory is shown in figure 13, and again good agreement is generally obtained. Indeed, it seems that the agreement improves as the Rossby number is increased, when compared with simulations Ai–vi and Bi–iv. Even in simulation Civ, in which the Froude number exceeds unity in the vortical region, the general form of the radiated wave field is captured by the Lighthill theory, although the fine details are not.

In figure 12, we see that in all cases A–C the pseudoenergy flux increases as the sixth power of the Froude number at small Froude number but, as the Froude number is

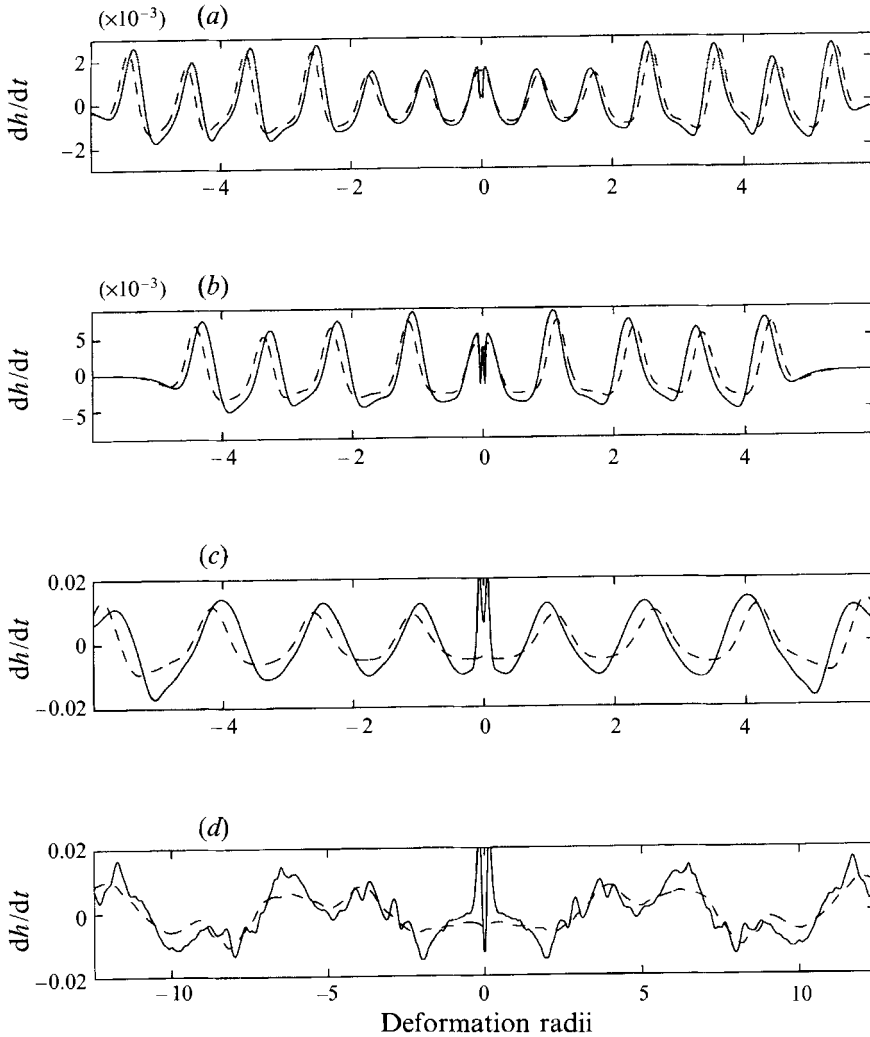


FIGURE 13. The x -averaged $\partial h/\partial t$ field at the termination of simulations C_i-iv (*a-d* respectively) (solid lines), and its reconstruction from the Lighthill convolution integral (dashed lines).

increased, the pseudoenergy flux increases less rapidly with increasing Froude number. It seems plausible from figure 12 that the very large-Rossby-number simulations C will exhibit an optimal Froude number for gravity wave radiation, in the same manner as simulations A and B, but that this value exceeds the values of Froude number investigated by the nonlinear simulations.

From this section, we may conclude that several of the features exhibited by the strips with a potential vorticity of 6 are robust features of cyclonic strip roll-up, subsequent nutation and gravity wave radiation. In particular, the nutation time increases super-exponentially with increasing Froude number. In general the pseudoenergy flux associated with the radiating gravity waves increases with the sixth power of the Froude number at small Froude number, but ultimately decreases as the Froude number is made very large, due to the increased nutation times, and consequently reduced fraction of the effective gravity wave source spectrum lying above the inertial frequency.

It is important to realize at this point that thus far only cyclonic strips have been investigated in this study. All cyclonic strips appear to exhibit similar behaviour, in respect of their vortex nutation times and pseudoenergy flux dependences upon the Froude number. In the remainder of this paper, we shall investigate gravity wave generation by anticyclonic vortex trains, and compare it with those found for cyclonic cases. The anticyclonic parameter space is divided into three parts: strips with positive potential vorticity, strips with negative potential vorticity, and the single case of a strip with a potential vorticity of zero. In the next section, §8, we consider strips with non-negative potential vorticity, and then proceed in the following section, §9, to consider strips with negative potential vorticity.

8. Anticyclonic strips with non-negative potential vorticity

In this section, two sets of simulations are presented, with strip potential vorticity values of 0.1 and 0, labelled D and E respectively.

Now, at low Froude number, the vortical flow is identical for all Rossby numbers, except that the timescale is set by the magnitude of the potential vorticity jump, with strips with small jumps evolving more slowly than those with larger jumps. However, we know from simulations A–C that a potential vorticity jump of at least 5 is required if the pseudoenergy flux is to exceed 10^{-6} at a Froude number of 0.1. In this section we are concerned with anticyclonic but positive potential vorticity in the strip. We are therefore restricted to strip potential vorticity values between 1 and 0, and hence potential vorticity jumps between 0 and 1. It follows that we must expect very weak gravity wave radiation at low Froude numbers when the potential vorticity in the strip is between 0 and 1. Consequently, it was decided to concentrate on a strip potential vorticity value of 0.1, which is quite small (i.e. δQ is quite large, given that the anticyclonic potential vorticity is required to be of the same sign as the background), and hence the flow will give rise to radiated gravity wave amplitudes which are as large as reasonably possible, without the strip potential vorticity being so close to zero that very large Froude numbers would be required to establish any significant differences between the two cases D and E.

Six simulations were performed with a strip potential vorticity of 0.1, with initial strip widths of 0.42, 0.84, 1.68, 3.36, 6.00 and 9.00, labelled Di–vi respectively. The vortical aspects of the dynamics in these simulations are similar to those found for simulations A–C. In common with the strips with cyclonic potential vorticity, the nutation times for experiments Di–vi, shown in figure 7, increase super-exponentially with increasing Froude number. However, agreement with the Lighthill theory is not found to be very good, even in the case Di, with a Froude number of only 0.2. Figure 14 shows the x -averaged $\partial h/\partial t$ field during simulation Di. Although the Lighthill reconstruction captures the essential features, on the whole it performs rather poorly, when compared with cyclonic experiments A–C at similar Froude numbers. Now, in classical aeroacoustics, only two lengthscales are present in the flow: the scale of the vortical motions, and the scale of the aeroacoustic waves which they generate. In the problem of gravity wave generation by vortical motions in a rotating frame, however, the Rossby deformation radius is an additional lengthscale, which is unity in the non-dimensionalization used here. The Lighthill theory assumes that the quadrupole source may be concentrated at a single point. If this is to be a good approximation, the scale of the vortical flow must be small with respect to the wavelength of the waves it generates, which is the usual low-Froude-number assumption, and must also be small compared with a Rossby deformation radius. It seems likely that the reason for the

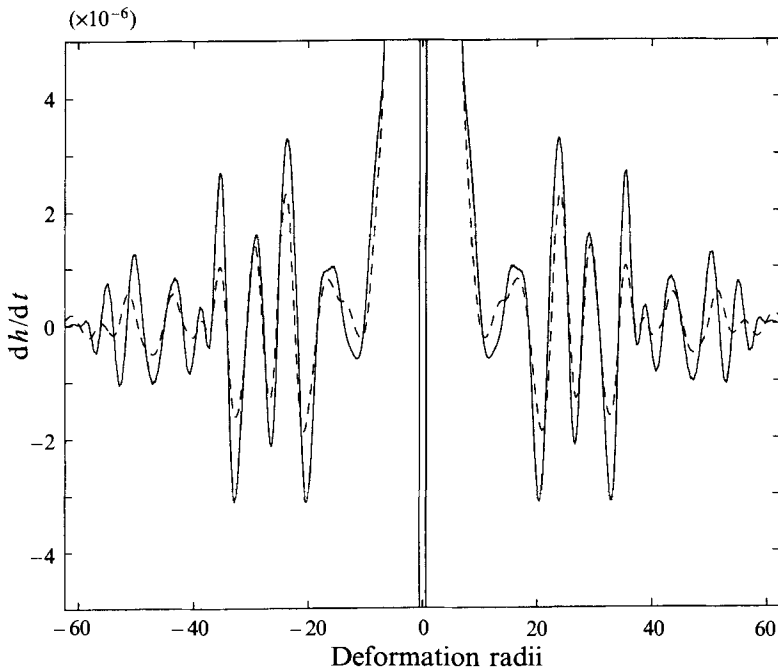


FIGURE 14. The x -averaged $\partial h/\partial t$ field at the termination of simulation D_i (solid line), and its reconstruction using the Lighthill convolution integral (dashed line).

rather poor agreement in figure 14 is that, although the Froude number of 0.2 is small, the initial width of the strip is 0.42, and therefore the vortices are not very small compared to a Rossby deformation radius.

In figure 15, the $\partial h/\partial t$ field is shown, at the time of most intense gravity wave emission, for simulations D_i–iv. As the Froude number increases, the nature of the gravity wave generation appears to change. At small Froude numbers, the generation appears to be a rather long-range effect, with gravity waves generated being of much longer wavelength than the scale of the vortical motions. At higher Froude numbers, however, the generation mechanism appears to be a rather more local effect, with gravity waves apparently being ‘launched’ off the edges of the vortices as they rotate. As the Froude number is increased still further, the gravity waves radiated by the vortex train lose their coherent x -independent structure. Figure 16 shows the gravity wave field during simulations D_v and D_{vi}. In comparison with simulations D_{iii} and D_{iv}, these gravity wave fields appear to be more arc-like, resembling radiation from point sources, rather than x -independent radiation from a line source exhibited at smaller Froude numbers.

Notice in figure 12 the dependence of the gravity wave pseudoenergy flux on the Froude number for experiments D_i–vi. As in the case of experiments A–C, experiments D_i–vi exhibit an optimal Froude number, above which the gravity wave pseudoenergy flux decreases as the Froude number is further increased. The existence of an optimal Froude number is almost certainly due to the fact that the vortex rotation times increase very rapidly with Froude number for Froude numbers close to unity, and hence the gravity waves are severely inhibited by the presence of background rotation.

It seems clear that the nature of the gravity wave radiation, and its ultimate limitation, is somewhat different in simulations D_i–vi from that found in simulations A–C. The gravity wave pseudoenergy flux appears to increase more rapidly with

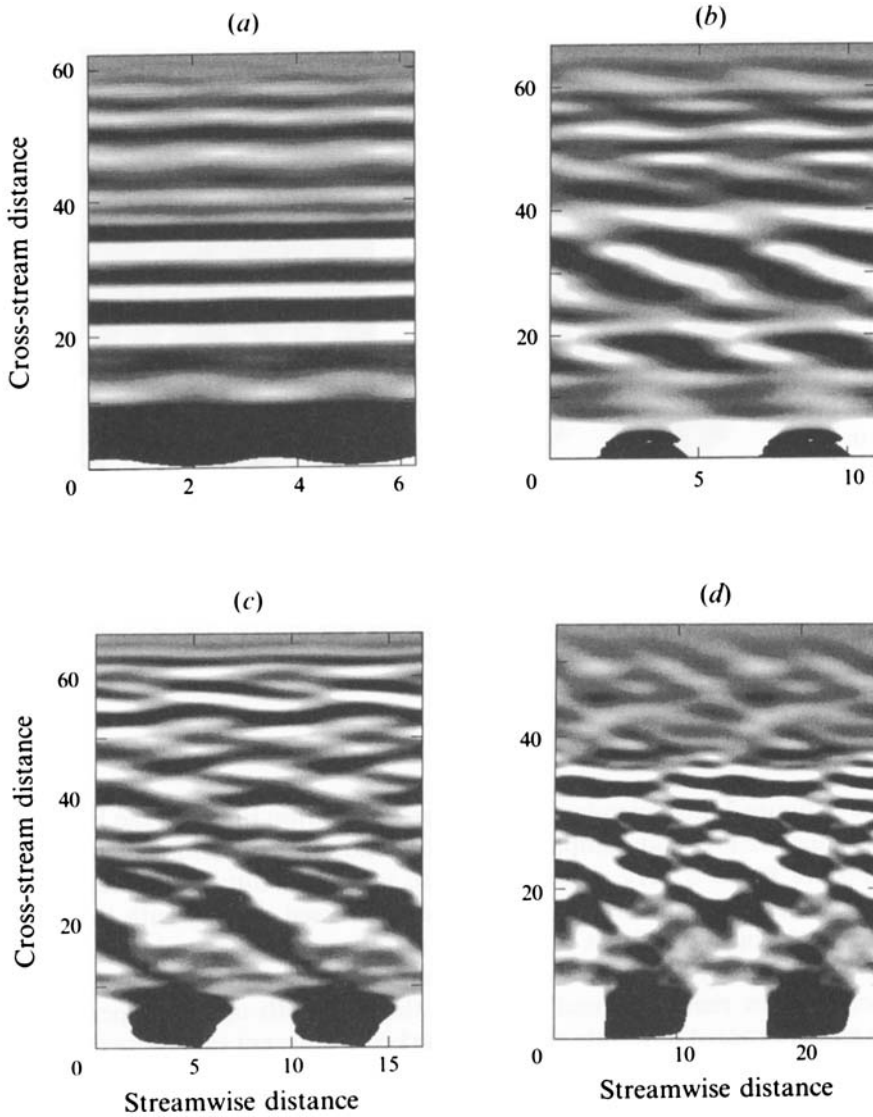


FIGURE 15. The $\partial h/\partial t$ field during the most active phase of gravity wave generation in simulations Di-iv (*a-d* respectively). Two periods of the model domain are shown.

Froude number, at moderate Froude numbers, and the transition from increasing gravity wave amplitudes to decreasing amplitudes as the Froude number is increased is much more abrupt than is found for cases A–C, with cyclonic potential vorticity in the strip. However, analysis in this case is difficult because, unlike the cyclonic simulations A–C, the vortices are very much larger, when compared with a Rossby deformation radius, at the critical Froude number at which the transition from increasing to decreasing pseudoenergy fluxes occurs. This means that the Lighthill theory is inapplicable in this limit, and an alternative analytical description of the flow has not been attempted.

The experiments with small positive potential vorticity in the strip are to be contrasted with experiments in which the potential vorticity in the strip is exactly zero. Five experiments were conducted with a strip potential vorticity of zero, with initial

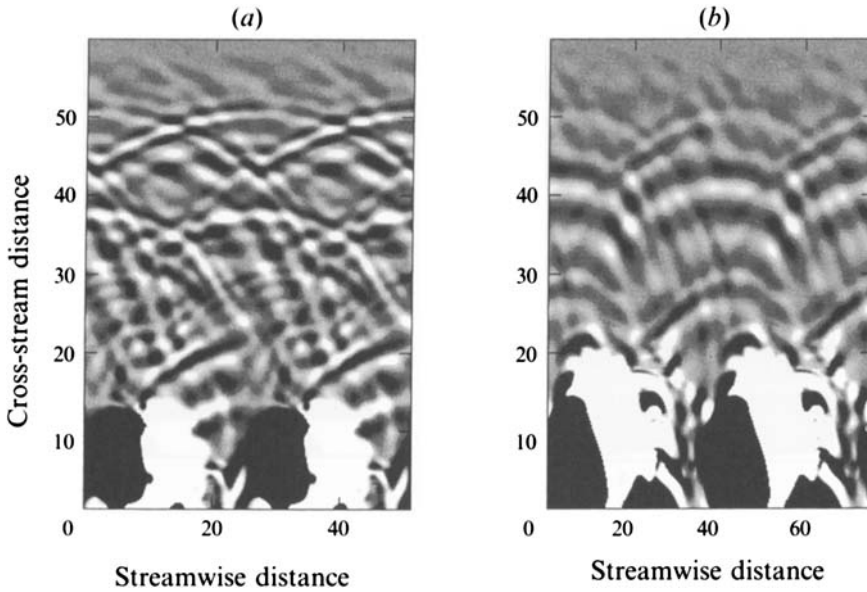


FIGURE 16. The $\partial h/\partial t$ field during simulations (a) Dv and (b) Dvi. Two periods of the model domain are shown.

strip widths of 0.42, 0.84, 1.26, 2.52 and 6.00. The experiments are labelled E_{i-v} respectively.

Notice in figure 7 the dependence of the vortex nutation times on the Froude number for experiments E_{i-v} , and compare them with those for experiments A–D. Although there appears to be a very gradual increase in vortex nutation times with Froude number in cases E_{i-v} , the behaviour is to be contrasted sharply with that found for a strip potential vorticity of just 0.1. A very significant difference in the nature of the vortical flows is thus observed between simulations D and E, although the general nature of the flow remains broadly similar: the strip rolls up into a periodic chain of vortices which proceed to nutate, albeit at markedly different rates between simulations D and E, without significant change of form.

The $\partial h/\partial t$ field during simulations E_{ii-v} is shown in figure 17. At lower Froude numbers, it appears to behave in a similar way to the wave field in simulations D, with the gravity waves being launched from the edges of the vortices as they rotate. However, as the Froude number is increased, the radiated wave field does not become less coherent, but rather the wave crests of the launched waves become progressively sharper, almost resembling shock waves in the highest-Froude-number simulation E_v .

The maximum pseudoenergy flux found in the gravity wave field in simulations E_{i-v} increases strongly with Froude number, in parallel with that observed for simulations D_{i-iv} (see figure 12). However, in case E the pseudoenergy flux increases with increasing Froude number apparently without bound, with the gravity wave field apparently becoming highly nonlinear, and somewhat shock-like, at the largest Froude numbers.

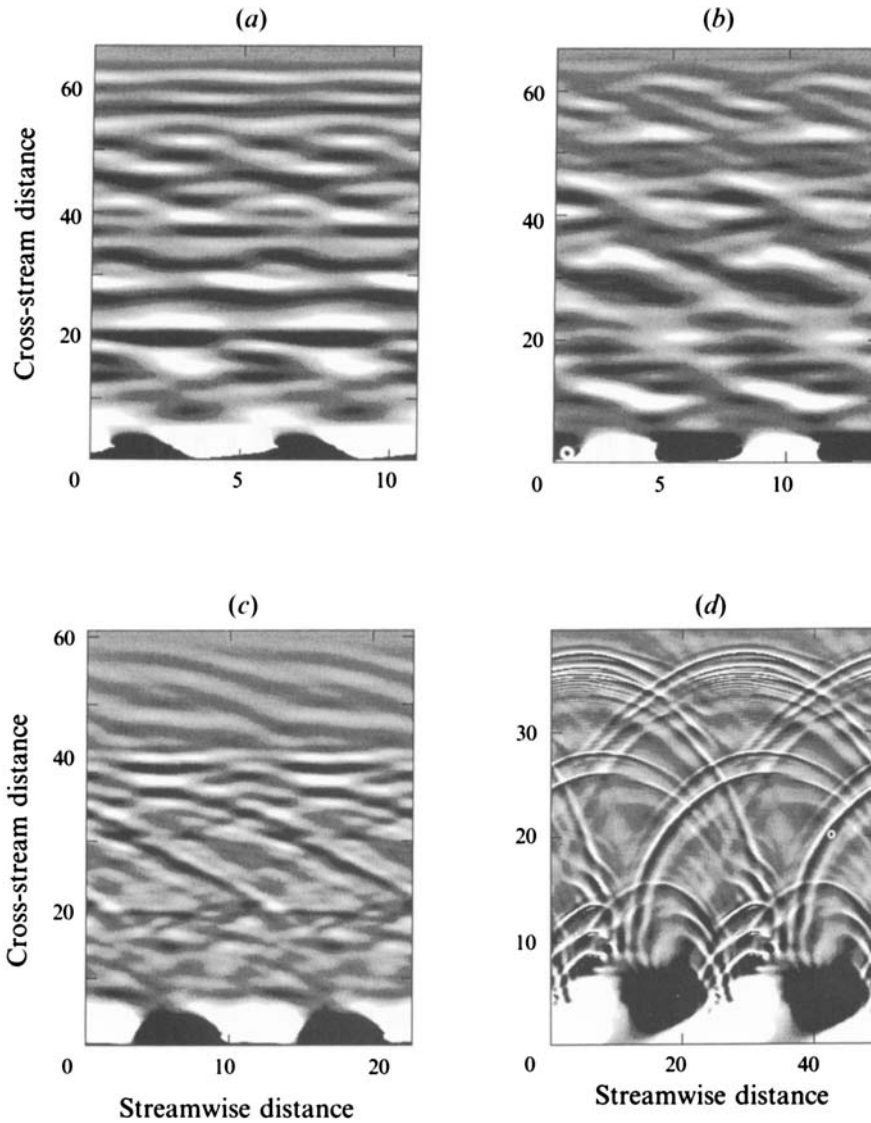


FIGURE 17. The $\partial h/\partial t$ field during simulations Eii-v (*a-d* respectively). Two periods of the model domain are shown.

9. Anticyclonic strips with negative potential vorticity

Having now classified the behaviour of the flows with non-negative potential vorticity, three further sets of simulations were undertaken to investigate gravity wave generation by vortex trains with negative potential vorticity. Strip potential vorticity values of -0.1 , -1.0 and -19.0 were investigated, with a range of strip widths in each case.

The experiments with a strip potential vorticity of -0.1 were performed for comparison with experiments Ei-v, in which the strip potential vorticity was zero, to investigate whether any additional effects occurred when slightly negative potential vorticity was present in the simulations. Six simulations were performed with a strip potential vorticity of -0.1 , labelled Fi-vi. Initial strip widths taken were 0.42, 0.84,

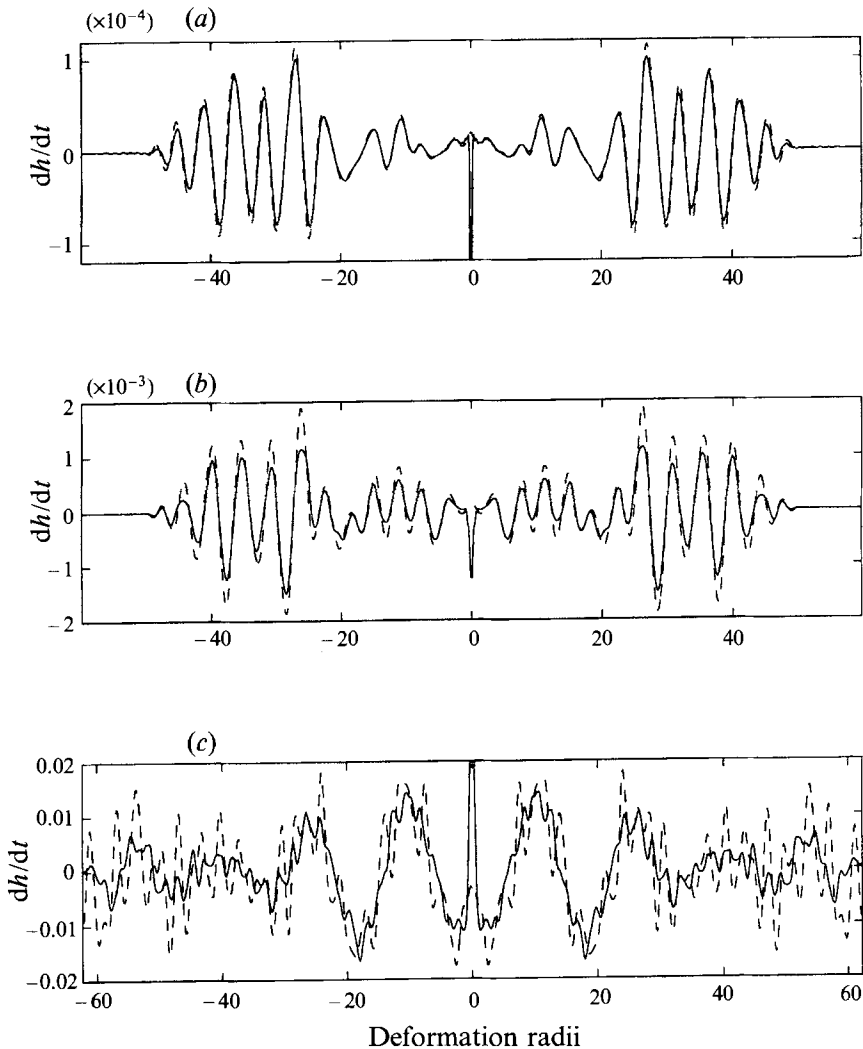


FIGURE 18. The x -averaged $\partial h/\partial t$ field at the termination of simulations Gi–iii (*a–c* respectively) (solid line), and its reconstruction from the Lighthill convolution integral (dashed line).

1.26, 1.68, 2.52 and 3.04. In figure 7, we see that the vortex nutation times for simulations Fi–vi are almost independent of Froude number, in common with Ei–v for strips with zero potential vorticity. The maximum pseudoenergy flux in the wave region, shown in figure 12, also appears to increase more rapidly than the sixth power of the Froude number, in common with Ei–v. The nature of the $\partial h/\partial t$ field in simulations Fi–vi broadly follows that for Ei–v. At small Froude numbers, the wave field consists of x -independent waves and waves with x -periodicity of one or two times the model domain. However, as the Froude number is increased, the x -dependence of the wave field increases, with shocks forming in cases Fv–vi (not shown). It seems reasonable to conclude that there is no appreciable difference between strips with zero potential vorticity, and strips with slightly negative potential vorticity.

Four simulations were then performed with a strip potential vorticity of -1.0 . The strips had initial strip widths of 0.07, 0.21, 0.42 and 0.63, and are labelled Gi–iv. Again, the vortex nutation times do not appear to change significantly with Froude number

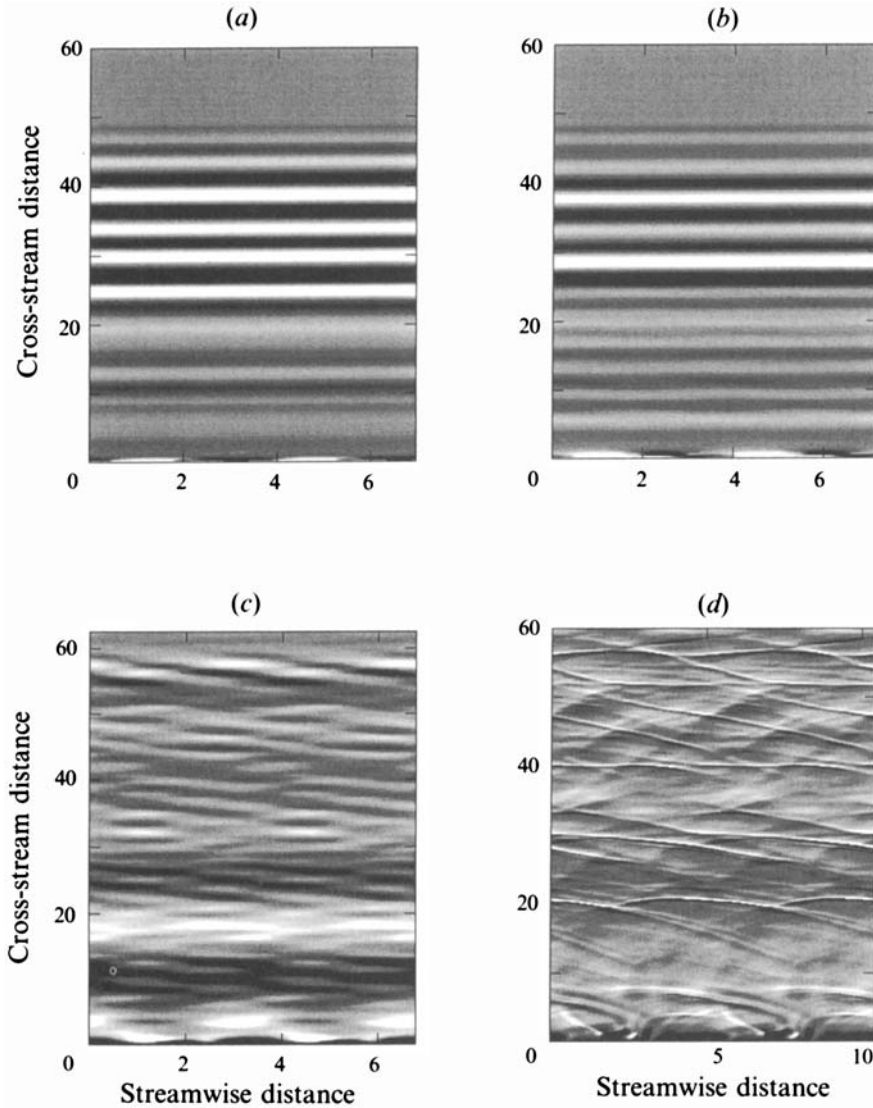


FIGURE 19. The $\partial h/\partial t$ field during the simulations Gi-iv (*a-d* respectively). Two periods of the model domain are shown.

(figure 7). The size of the vortices compared to a Rossby deformation radius is now much smaller than was the case in simulations D, E and F, with the largest initial strip width being 0.63, only 50% wider than the smallest initial strip width in simulations D, E and F. Consequently, the Lighthill theory is significantly more successful at reconstructing the wave field. The x -averaged $\partial h/\partial t$ field, and its reconstruction from the Lighthill source term, is shown for simulations Gi-iii in figure 18, and good agreement is obtained for initial strip widths of 0.07 and 0.21.

However, in line with experiments E and F, the character of the wave field departs significantly from that of linear waves as the Froude number is increased. In figure 19, the $\partial h/\partial t$ field is shown at the end of each simulation for the cases Gi-iv. In the first three cases the wave field appears to be well described by linear waves. At small Froude

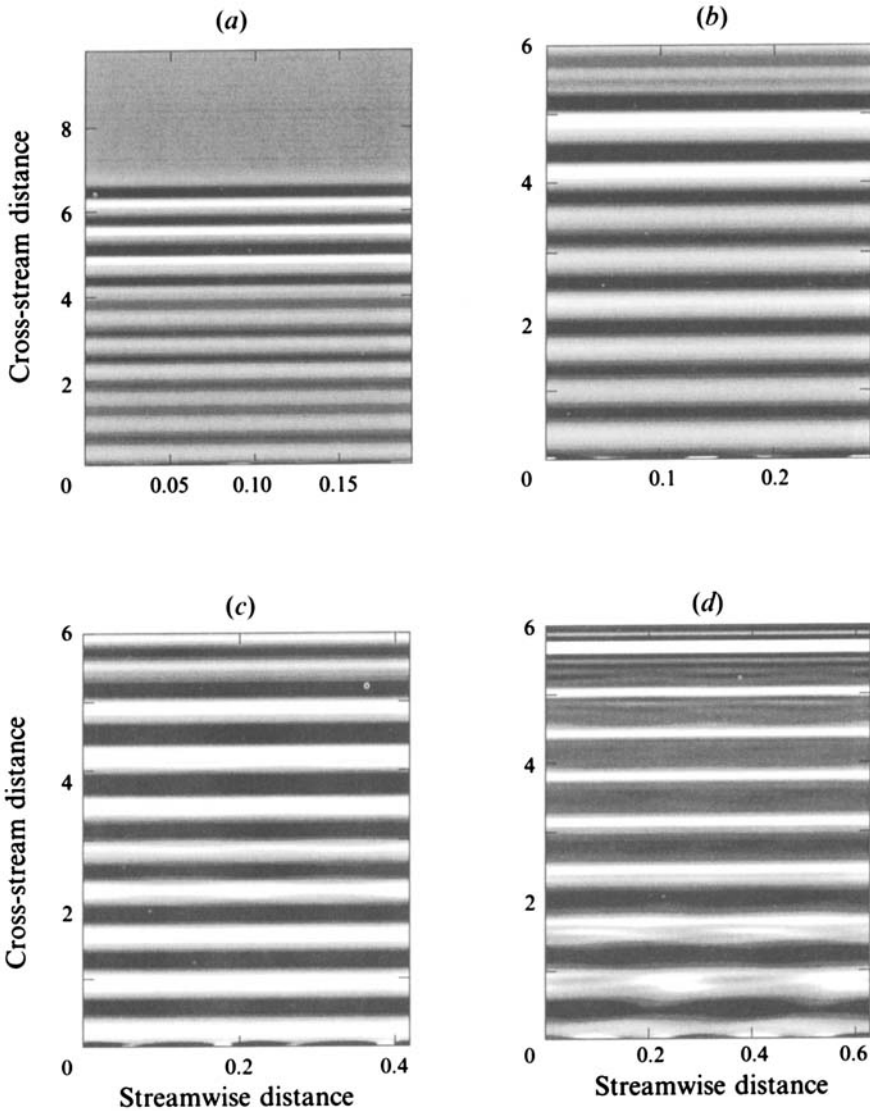


FIGURE 20. The $\partial h / \partial t$ field at the termination of simulations HI-iv (*a-d* respectively). Two periods of the model domain are shown.

numbers the wave field is dominated by x -independent waves, with x -dependence increasing with increasing Froude number in simulations GI-iii. Indeed, linear wave-like motions in the gravity wave field are a pre-requisite for good agreement with the Lighthill theory, observed in figures 18(*a*) and 18(*b*), which assumes a linear radiating wave field. In simulation Giv, however, the character of the wave field differs markedly from linear wave-like motions, with shock waves appearing in the radiating gravity wave field. In common with simulations Ev and Fv, the shocks in simulation Giv also appear to originate in the vortical region itself, although they appear to be somewhat sharper in this case than in the other two. At this point, however, it should be recognized that the discretization scheme is not designed to capture shocks, and any quantitative discussion of differences between shocks is inappropriate. If the details of

the shock waves generated are of interest, then the experiments would have to be repeated using a shock-capturing scheme. However, with meteorological applications in mind, it should be recalled that continuously stratified three-dimensional flows with negative potential vorticity are inertially unstable (Hoskins 1974), and these extreme cases in which flow with negative potential vorticity generates shock waves are therefore unlikely to be of practical meteorological interest.

We can see from figure 12 that, at small Froude numbers, the pseudoenergy flux is increasing as the sixth power of the Froude number in this case. The increase then appears to become more rapid as the Froude number increases, in common with other anticyclonic simulations D–F, in which it appears that the pseudoenergy flux increases more rapidly than the sixth power of the Froude number. These do, of course, differ from the cyclonic simulations, in which the pseudoenergy flux never increased more rapidly than the sixth power of the Froude number.

Finally, four simulations were performed with a strip potential vorticity of -19.0 . These simulations were performed for comparison with simulations Ci–iv, in which the strip potential vorticity was taken to be 21.0 . Consequently, at small Froude numbers, the dynamics of the strips should be identical in the two cases, with the magnitude of the potential vorticity jump being equal to 20 in both cases. Strip widths of 0.007 , 0.013 , 0.021 and 0.031 were taken, and the simulations are labelled Hi–iv respectively.

From figure 7, it can clearly be seen that when there is negative potential vorticity in the strip the nutation times remain almost constant as the Froude number is increased, whereas in the case of positive potential vorticity in the strip the nutation times increase super-exponentially.

In figure 20 the $\partial h/\partial t$ field is shown at the termination of simulations Hi–iv, and in figure 21 the comparison with the Lighthill theory is shown. The agreement seems quite good at small Froude numbers, but not as good as in simulations Ci–iv, even though the waves remain nearly independent of x .

Now consider the peak pseudoenergy flux in the gravity wave far field, shown in figure 12. One can see that, although both sets of simulations are initially quite similar, as the Froude number is increased the simulations Hi–iv, with negative potential vorticity in the strip, radiate gravity waves much more strongly than the corresponding cyclonic simulations with the same magnitude of potential vorticity difference between the strip and the background. Significantly, the pseudoenergy flux increases as the sixth power of the Froude number throughout simulations Hi–iv, and the faster-than-sixth power increase in pseudoenergy flux, observed for less anticyclonic simulations, does not appear to be present here, consistent with the vortical flow in this case being confined to a region small compared with a deformation radius, and therefore in a region in which (14) should apply.

When comparing the x -averaged $\partial h/\partial t$ field with its reconstruction from the Lighthill convolution integral (6), it is of interest to note that, while in most cases the maxima of the actual and reconstructed field coincide, in simulations C and H, shown in figures 13 and 21 respectively, the maxima appear to be offset. In figure 13, the maxima of the field obtained by reconstruction from (6) appear to lead those obtained by direct numerical simulation, whereas in figure 21 they tend to lag those obtained by direct numerical simulation. The reason is that the Lighthill theory assumes that the wave phase speed c_0 is constant everywhere. However, the vortical flow adjusts to rest over the scale of a Rossby deformation radius. In most cases, the radiated waves are of long wavelength compared with a Rossby deformation radius. However, as the potential vorticity in the strip increases, so the frequency of the vortical motion increases, and hence the wavelength of the radiated waves decreases. In cases C and H,

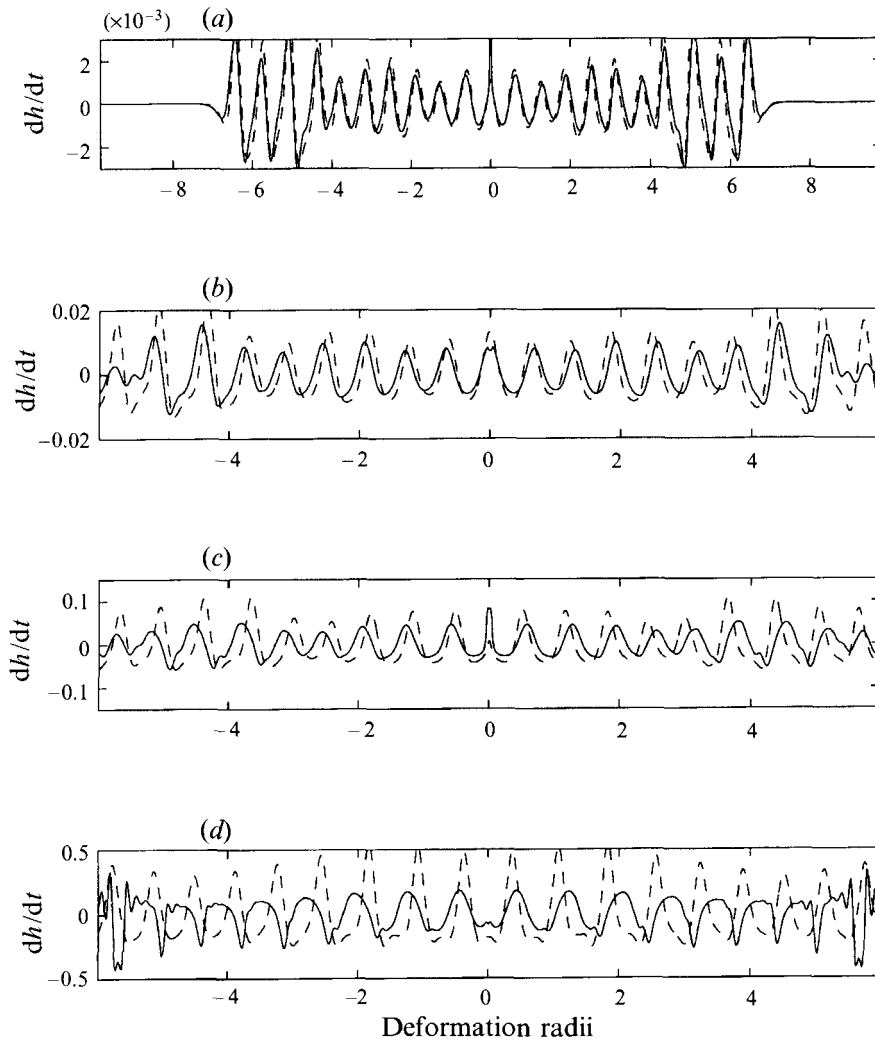


FIGURE 21. The x -averaged $\partial h/\partial t$ field at the termination of simulations Hi-iv (a - d respectively) (solid lines), and its reconstruction from the Lighthill convolution integral (dashed lines).

the wavelength of the radiated waves is of the order of a deformation radius, and therefore they may be significantly affected during their propagation through the region over which the flow relaxes and adjusts to rest. In the cyclonic case C, the layer depth is less near the strip than at infinity, and the waves will tend to propagate more slowly there. Hence, the waves predicted by (6) will tend to lead those obtained by direct numerical simulation. Conversely, in the anticyclonic case H, the layer depth is greater near the strip than at infinity, and the waves will propagate more quickly there. Hence, the waves predicted by (6) will tend to lag those obtained by direct numerical simulation, in agreement with what is found in figures 13 and 21.

10. Discussion

Gravity wave radiation by a train of vortices in shallow water has been studied by direct numerical simulation. The dependence of the gravity waves radiated upon the Froude and Rossby numbers was investigated.

Arguably the most surprising result is that, for cyclonic vortices at a Rossby number of 5, increasing the Froude number above 0.35 can lead to a decrease in the amplitude of the gravity waves radiated by the vortex train. This is in contrast to laboratory experiments, and the numerical experiments of Lele & Ho (1994) for a non-rotating gas, in which the acoustic wave amplitudes scaled according to the Lighthill theory for Mach numbers of up to 0.6 or so.

A summary of the results, showing the dependence of the radiated pseudoenergy flux on the Froude number for various Rossby numbers is shown in figure 12. One can see that, in general, whereas positive potential vorticity trains tended to exhibit an 'optimal' Froude number for gravity wave generation, the amplitude of gravity waves radiated by negative potential vorticity trains increases apparently without bound as the Froude number increases.

Typical vortex nutation times for all experiments are shown in figure 7. One can see that nutation times increase super-exponentially with Froude number for all cyclonic vortex simulations, A–C, and also for anticyclonic simulations D (when the potential vorticity in the strip is strictly positive). As a result, the x -averaged pseudoenergy flux of the radiated gravity waves never exceeds about 10^{-4} in simulations A–D, as the inhibiting effect of the inertial frequency becomes increasingly significant as the nutation times increase. However, when the potential vorticity in the strip is zero or negative, there does not appear to be any significant dependence of the nutation time upon the Froude number, and the radiated gravity wave fluxes apparently increase without bound.

The most likely explanation for this difference lies in the range of interaction for vortical flows in rotating shallow water, which is given as $(Qf/g)^{-1/2}$ for parallel flow, with some modifications for axisymmetric flow (see, for example, Hoskins *et al.* 1985). Thus, if $Qf > 0$, as it is in cases A–D, it follows that, as the extent of the vortices is increased above their interaction range, the radius of curvature of the flow will become large compared with the internal interaction range for the vortex. At this point, the flow in the vortices may appear locally like a parallel flow, with jets on the edge of the vortex and a region of relative calm in the centre. The vortices may then be expected to become less unsteady, as the jets resemble locally isolated parallel flows. This effect is not present in the case of $Qf \leq 0$, corresponding to cases E–H, and hence the vortices would not be expected to nutate more slowly as their magnitude increases.

To check that this explanation is plausible, we consider cross-stream sections of $|\mathbf{u}|$ through vortices with potential vorticity of 0.1 and 0. We examine two cases from each: two at small Froude number (Di and Ei respectively), and two at large Froude number (Dvi and Ev respectively). In all cases, the cross-section is taken at a time in the simulation when the vortices are aligned with their major axis parallel to the initial streamwise direction, several nutations after the initial roll-up of the strip, and in each case the cross-section passes through the centre of the vortex.

In figure 22(a), the cross-sections of $|\mathbf{u}|$ are shown as a function of cross-stream coordinate for vortices with small Froude number (cases Di and Ei). Notice that in these two cases the shear rate $d|\mathbf{u}|/dy$ depends only upon the relative magnitude of the potential vorticity contrast with the background unit potential vorticity. In figure 22(b), the cross-sections of $|\mathbf{u}|$ are as a function of cross-stream coordinate at large Froude number (cases Dvi and Ev). In these cases, the shear rate for the case $Q = 0$ is almost unchanged from its value at small Froude number, whereas the shear rate for the case $Q = 0.1$ has reduced significantly. Notice in particular that in the case $Q = 0.1$ $d|\mathbf{u}|/dy$ is approximately zero at $y = 0$, and there is a region of non-zero cross-stream extent in which $|\mathbf{u}|$ is small, unlike the case of $Q = 0$. This is consistent with the notion

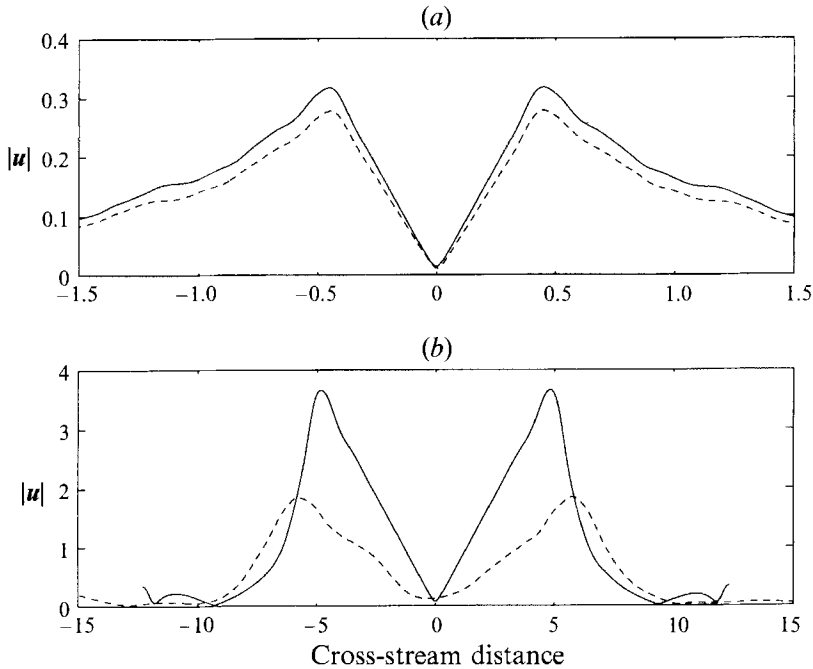


FIGURE 22. Cross-stream sections of $|u|$ for $Q = 0.1$ (dashed line) and $Q = 0$ (solid line): (a) Di, Ei; (b) Dvi, Ev.

that the vortex in the case Dvi is large compared with its internal deformation scale, and therefore has a region of relative calm at its centre, whereas the vortices in case Ev are vigorous throughout their core. However, although figure 22 demonstrates that there is a qualitative difference between positive and zero potential vorticity in vortices at large Froude number, there does not seem to be any straightforward way to predict how the nutation time should scale with Froude number. Indeed the magnitude of the effect of an internal deformation scale on the nutation time appears to be quite large, with a seven-fold increase in the nutation time between Ev and Dvi.

Some asymmetry between cyclones and anticyclones at Rossby and Froude numbers of order unit has been observed in numerical simulations by Polvani *et al.* (1994), where the geometry of the flow is doubly periodic, and the initial vorticity field is random. The flow is balanced using the nonlinear balance equations (McWilliams 1985). In time, large coherent vortices develop, and at small Froude number there is symmetry between cyclonic and anticyclonic vortices. At larger Froude numbers, however, the flow is dominated by large coherent anticyclones, with much of the cyclonic potential vorticity smeared out into thin filaments. In some simulations, shock waves have been observed, emanating from the anticyclones. Polvani *et al.*'s simulations are in agreement with the results presented here, in that anticyclones are more vigorous features than cyclones in shallow-water dynamics at order-one Froude numbers, and are capable of generating shock waves in the gravity wave field at sufficiently large Froude number. Clearly some further analysis is warranted to investigate in more detail the distinction between cases where the potential vorticity in the vortices is of the same sign as the background, and those where it is of the opposite sign.

Finally, we recall that this study was motivated, in part, by the observation by Norton (1988) and McIntyre & Norton (1994) that gravity waves of large amplitude were generally not generated by the vortical motions in their disturbed polar vortex

simulations. Now, in polar vortex simulations, the majority of the vortical motions are cyclonic, and the potential vorticity is all of one sign throughout the hemispherical domain. Consequently, they are not able to access the regime of zero and negative potential vorticity, which has been demonstrated in this paper to be the regime in which the strongest gravity wave generation might be expected. On the other hand, regions of negative potential vorticity are likely to be unstable to inertial instability (Hoskins 1974). Therefore, the results from simulations F–H in the present study should be taken as complementary to those from simulations A–D. They should be regarded as adding weight to the theory that it is the presence of an internal interaction range which reduces the unsteadiness at large Froude numbers in A–D, but it should not be inferred that regions of negative potential vorticity are likely to be sites of intense gravity wave generation by the mechanism discussed in this paper.

This work was carried out while the author was a PhD student, supported by a studentship from the United Kingdom Natural Environment Research Council. Professor M. E. McIntyre made several helpful suggestions as the work progressed. The extension of the Lighthill theory to rotating shallow water was first performed by W. A. Norton (unpublished). Helpful discussions with B. J. Hoskins, R. Rotunno, R. Saravanan and J. F. Scinocca are gratefully acknowledged. Anonymous reviewers made helpful suggestions for the improvement of the manuscript.

REFERENCES

- ALLEN, J. S., BARTH, J. A. & NEWBERGER, P. A. 1990 On intermediate models for barotropic continental shelf and slope flow fields. Part III: Comparison of numerical model solutions in periodic channels. *J. Phys. Oceanogr.* **20**, 1949–1973.
- ASSELIN, R. 1972 Frequency filter for time integrations. *Mon. Wea. Rev.* **100**, 487–490.
- BARTH, J. A., ALLEN, J. S. & NEWBERGER, P. A. 1990 On intermediate models for barotropic continental shelf and slope flow fields. Part II: Comparison of numerical model solutions in doubly periodic domains. *J. Phys. Oceanogr.* **20**, 1044–1076.
- BRIDGES, J. & HUSSAIN, A. K. M. F. 1992 Direct evaluation of aeroacoustic theory in a jet. *J. Fluid Mech.* **240**, 469–501.
- CROW, S. C. 1970 Aerodynamic sound generation as a singular perturbation problem. *Stud. Appl. Maths* **49**, 21–44.
- FLOWCS WILLIAMS, J. E. 1969 Hydrodynamic noise. *Ann. Rev. Fluid Mech.* **1**, 197–222.
- FORD, R. 1993 Gravity wave generation by vortical flows in a rotating frame. PhD thesis, University of Cambridge.
- FORD, R., MCINTYRE, M. E. & NORTON, W. A. 1994 Balance and the slow quasi-manifold: some explicit results. *J. Atmos. Sci.* (submitted).
- HAYNES, P. H. 1988 Forced, dissipative generalizations of finite-amplitude wave-activity conservation relations for zonal and non-zonal basic flows. *J. Atmos. Sci.* **45**, 2352–2362.
- HAYNES, P. H. 1989 The effect of barotropic instability on the nonlinear evolution of a Rossby wave critical layer. *J. Fluid Mech.* **207**, 231–266.
- HO, C.-M. & HUERRE, P. 1984 Perturbed free shear layers. *Ann. Rev. Fluid Mech.* **16**, 365–424.
- HOSKINS, B. J. 1974 The role of potential vorticity in symmetric stability and instability. *Q. J. R. Met. Soc.* **100**, 480–482.
- HOSKINS, B. J., MCINTYRE, M. E. & ROBERTSON, A. W. 1985 On the use and significance of isentropic potential-vorticity maps. *Q. J. R. Met. Soc.* **111**, 877–946.
- KAMBE, T. & MINOTA, T. 1981 Sound radiation from vortex systems. *J. Sound Vib.* **74**, 61–72.
- KAMBE, T. & MINOTA, T. 1983 Acoustic wave radiated by head-on collision of two vortex rings. *Proc. R. Soc. Lond. A* **386**, 277–308.
- LEGRAS, B. & DRITSCHEL, D. G. 1993 A comparison of the contour surgery and pseudo-spectral methods. *J. Comput. Phys.* **104**, 287–302.

- LELE, S. K. & HO, C.-M. 1994 Acoustic radiation from temporally evolving free shear layers. *J. Fluid Mech.* (submitted).
- LIGHTHILL, M. J. 1952 On sound generated aerodynamically, I. General theory. *Proc. R. Soc. Lond. A* **211**, 564–587.
- LIGHTHILL, M. J. 1954 On sound generated aerodynamically, II. Turbulence as a source of sound. *Proc. R. Soc. Lond. A* **222**, 1–32.
- LUSH, P. A. 1971 Measurements of subsonic jet noise and comparison with theory. *J. Fluid Mech.* **46**, 477–500.
- MCINTYRE, M. E. & NORTON, W. A. 1994 Potential vorticity inversion on a hemisphere. *J. Atmos. Sci.* (submitted).
- MCINTYRE, M. E. & SHEPHERD, T. G. 1987 An exact local conservation theorem for finite amplitude disturbances to non-parallel shear flows, with remarks on Hamiltonian structure and Arnol'd's stability theorems. *J. Fluid Mech.* **181**, 527–565.
- MCWILLIAMS, J. C. 1985 A uniformly valid model spanning the regimes of geostrophic and isotropic, stratified turbulence: balanced turbulence. *J. Atmos. Sci.* **42**, 1773–1774.
- MCWILLIAMS, J. C., GENT, P. R. & NORTON, N. J. 1986 The evolution of balanced, low-mode vortices on the β -plane. *J. Phys. Oceanogr.* **16**, 838–855.
- MINOTA, T. & KAMBE, T. 1986 Observations of acoustic emission from head-on collision of two vortex rings. *J. Sound Vib.* **111**, 51–59.
- MOORE, C. J. 1977 The role of shear-layer instability waves in jet exhaust noise. *J. Fluid Mech.* **80**, 321–367.
- MORSE, P. M. & FESHBACH, H. 1953 *Methods of Mathematical Physics II*. McGraw-Hill.
- NORTON, W. A. 1988 Balance and potential vorticity inversion in atmospheric dynamics. PhD thesis, University of Cambridge.
- POLVANI, L. M., MCWILLIAMS, J. C., SPALL, M. A. & FORD, R. 1994 The coherent structures of shallow-water turbulence: deformation radius effects, cyclone/anticyclone asymmetry and gravity-wave generation. *Chaos* **4**, 177–186.
- POZRIKIDIS, C. & HIGDON, J. L. L. 1985 Nonlinear Kelvin–Helmholtz instability of a finite vortex layer. *J. Fluid Mech.* **157**, 225–263.
- ROBERT, A. J. 1966 The integration of a low order spectral form of the primitive meteorological equations. *J. Met. Soc. Japan* **44**, 237–245.
- WAUGH, D. W. & DRITSCHEL, D. G. 1991 The stability of filamentary vorticity in two-dimensional geophysical vortex-dynamics models. *J. Fluid Mech.* **231**, 575–598.
- WEBSTER, R. B. 1970 Jet noise simulation on shallow water. *J. Fluid Mech.* **40**, 423–432.